Article

Cell Stem Cell

FOXO3-Engineered Human ESC-Derived Vascular Cells Promote Vascular Protection and Regeneration

Graphical Abstract

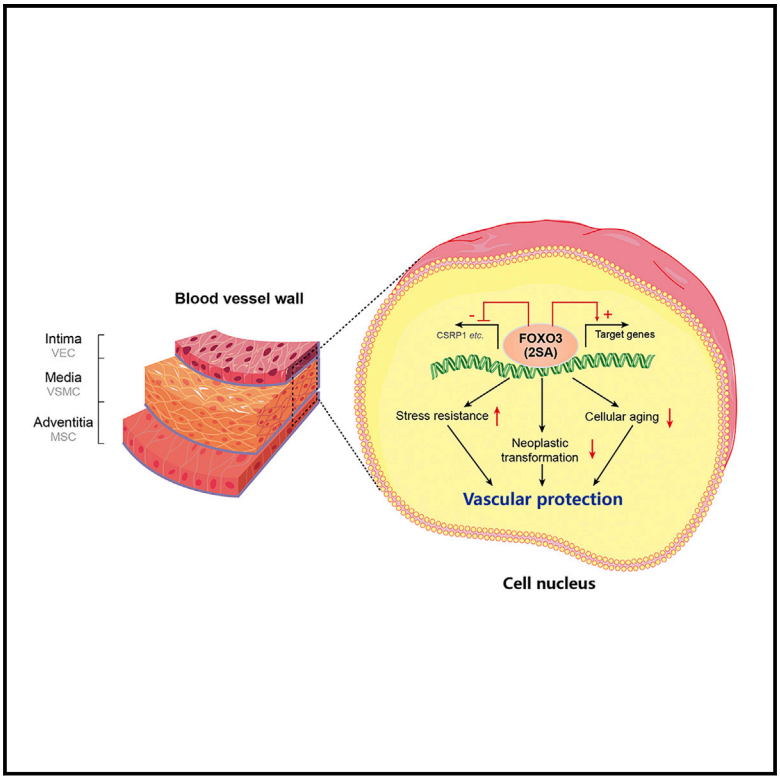

Authors

Pengze Yan, Qingqing Li, Lixia Wang, ..., Jing Qu, Fuchou Tang, Guang-Hui Liu

Correspondence

qujing@ioz.ac.cn (J.Q.), tangfuchou@pku.edu.cn (F.T.), ghliu@ibp.ac.cn (G.-H.L.)

In Brief

Yan et al. switch a pair of nucleotides in *FOXO3* and endow human vascular cells with the ability to resist senescence, stress, and tumorigenesis. This study demonstrates that activated FOXO3 contributes to the maintenance of vascular homeostasis, providing a strategy for the generation of higher-quality transplants for stem cell-based therapy.

Highlights

- Recoding of two nucleotides in *FOXO3* gene is sufficient to activate FOXO3 activity
- Genetic activation of FOXO3 reinforces the homeostasis of human vascular cells
- FOXO3-enhanced vascular cells promote revascularization after ischemic surgery
- FOXO3-activated human stem cells are resistant to oncogenic transformation

Yan et al., 2019, Cell Stem Cell *24*, 447–461
March 7, 2019
https://doi.org/10.1016/j.stem.2018.12.002

CellPress

Cell Stem Cell
Article

FOXO3-Engineered Human ESC-Derived Vascular Cells Promote Vascular Protection and Regeneration

Pengze Yan,[1,2,4,15] Qingqing Li,[3,15] Lixia Wang,[1,4] Ping Lu,[3] Keiichiro Suzuki,[8,9,16] Zunpeng Liu,[2,4] Jinghui Lei,[6] Wei Li,[6] Xiaojuan He,[6] Si Wang,[1] Jianjian Ding,[14] Piu Chan,[6] Weiqi Zhang,[1,4,6,7,16] Moshi Song,[4,5,7,16] Juan Carlos Izpisua Belmonte,[10,16] Jing Qu,[2,4,7,*] Fuchou Tang,[3,11,12,*] and Guang-Hui Liu[1,4,6,7,13,17,*]

[1]National Laboratory of Biomacromolecules, CAS Center for Excellence in Biomacromolecules, Institute of Biophysics, Chinese Academy of Sciences, Beijing 100101, China
[2]State Key Laboratory of Stem Cell and Reproductive Biology, Institute of Zoology, Chinese Academy of Sciences, Beijing 100101, China
[3]Beijing Advanced Innovation Center for Genomics and Biomedical Pioneering Innovation Center, College of Life Sciences, Peking University, Beijing 100871, China
[4]University of the Chinese Academy of Sciences, Beijing 100049, China
[5]State Key Laboratory of Membrane Biology, Institute of Zoology, Chinese Academy of Sciences, Beijing, 100101, China
[6]Advanced Innovation Center for Human Brain Protection, National Clinical Research Center for Geriatric Disorders, Xuanwu Hospital Capital Medical University, Beijing 100053, China
[7]Institute for Stem Cell and Regeneration, Chinese Academy of Sciences, Beijing 100101, China
[8]Institute for Advanced Co-Creation Studies, Graduate School of Engineering Science, Osaka University, Osaka 560-8531, Japan
[9]Graduate School of Engineering Science, Osaka University, Osaka 560-8531, Japan
[10]Gene Expression Laboratory, Salk Institute for Biological Studies, 10010 North Torrey Pines Road, La Jolla, CA 92037, USA
[11]Peking-Tsinghua Center for Life Sciences, Peking University, Beijing 100871, China
[12]Ministry of Education Key Laboratory of Cell Proliferation and Differentiation, Beijing 100871, China
[13]Beijing Institute for Brain Disorders, Beijing 100069, China
[14]Army Diagnosis and Treatment Center for Oral Disease, 306th Hospital of the PLA, Beijing 100101, China
[15]These authors contributed equally
[16]Senior author
[17]Lead Contact
*Correspondence: qujing@ioz.ac.cn (J.Q.), tangfuchou@pku.edu.cn (F.T.), ghliu@ibp.ac.cn (G.-H.L.)
https://doi.org/10.1016/j.stem.2018.12.002

SUMMARY

FOXO3 is an evolutionarily conserved transcription factor that has been linked to longevity. Here we wanted to find out whether human vascular cells could be functionally enhanced by engineering them to express an activated form of FOXO3. This was accomplished via genome editing at two nucleotides in human embryonic stem cells, followed by differentiation into a range of vascular cell types. FOXO3-activated vascular cells exhibited delayed aging and increased resistance to oxidative injury compared with wild-type cells. When tested in a therapeutic context, FOXO3-enhanced vascular cells promoted vascular regeneration in a mouse model of ischemic injury and were resistant to tumorigenic transformation both *in vitro* and *in vivo*. Mechanistically, constitutively active FOXO3 conferred cytoprotection by transcriptionally downregulating *CSRP1*. Taken together, our findings provide mechanistic insights into FOXO3-mediated vascular protection and indicate that FOXO3 activation may provide a means for generating more effective and safe biomaterials for cell replacement therapies.

INTRODUCTION

Proper functioning of the cardiovascular system is essential for maintaining tissue homeostasis and for promoting maximal organismal lifespan. Age-associated cardiovascular dysfunction impairs the ability of this system to deliver nutrients and oxygen to various organs (Omae et al., 2013). Vascular aging is often associated with endothelial dysfunction, reduced vascular elasticity, and decreased potential for vascular repair as well as increased secretion of proinflammatory cytokines (Harvey et al., 2015; Laurent, 2012; Mikael et al., 2017).

Forkhead box O3 (FOXO3) is an evolutionarily conserved longevity factor (Martins et al., 2016; van der Horst and Burgering, 2007). Certain *FOXO3* SNPs correlate with human longevity in diverse human populations (Chung et al., 2010; Flachsbart et al., 2018; He et al., 2014; Willcox et al., 2008). Longevity-related *FOXO3* polymorphisms are also associated with a lower-than-average prevalence of cardiovascular diseases (CVDs) in long-lived humans (Willcox et al., 2008). Although it remains unclear how human genetic variations of *FOXO3* prolong the human lifespan mechanistically, considerable advances have been made in revealing the cellular function of FOXO3. As a member of the O class of forkhead box transcription factors, FOXO3 is a major downstream effector of the phosphatidylinositol 3-kinase (PI3K)/Akt signaling pathway, participating in various cellular processes, including cell proliferation,

oxidative resistance, DNA damage repair, cell apoptosis, cellular senescence, and stem cell homeostasis (Brunet et al., 2004; Martins et al., 2016; Morris et al., 2015; Paik et al., 2007; Santos et al., 2014; Tsai et al., 2008). Akt-mediated phosphorylation of FOXO3 at three classical sites, Thr32, Ser253, and Ser315, promotes FOXO3 translocation to the cytoplasm (via its binding to a 14-3-3 protein) and subsequent ubiquitination and degradation. When Akt activity is inhibited or FOXO3 phosphorylation sites are mutated, FOXO3 is retained in the nucleus, where it continues to regulate target gene transcription (Brunet et al., 1999).

Human blood vessels are primarily composed of vascular endothelial cells (VECs), vascular smooth muscle cells (VSMCs), mesenchymal stem cells (MSCs), etc. These represent the major cell types within the *intima*, *media*, and *adventitia* layers of blood vessels, respectively (Chen et al., 2014; Crisan et al., 2008; Murray et al., 2014; Zengin et al., 2006). Loss-of-function studies have shown that FOXO3 helps to maintain homeostasis for a diverse array of vascular cell types (Deng et al., 2015; Zhang et al., 2017). However, it remains unexplored whether the FOXO3 pathway can be targeted to generate human stem cells with enhanced utility in cell-based therapies.

Recent advances in targeted gene editing have shown great potential for use in stem cell replacement therapy (Maguire, 2016; Mahla, 2016; Tompkins et al., 2015; Yang et al., 2017). Targeted gene editing facilitates accurate manipulation of the human genome, making it possible to obtain autologous "healthy" stem cells via correction or deletion of disease-causing mutations found in patient-derived somatic cells. To date, somatic stem cells derived from patients with various genetic diseases have been corrected (Schwank et al., 2013; Wang et al., 2017). However, the efficacy of this therapeutic approach is far from optimal, based on the limited expansion of somatic stem cells *in vitro* and the rapid stress-induced decay of stem cells *in vivo*. Further, safety concerns regarding the risk of stem cell or gene editing-associated carcinogenesis impede the widespread application of these technologies (Azene et al., 2014; Ihry et al., 2018; Liu et al., 2014). Therefore, it is urgent to generate stem cell grafts that exhibit increased resistance to stress and reduced tumorigenic potential.

Here we used genome editing to replace two FOXO3 phosphorylation sites (Ser253 and Ser315) with alanines ($FOXO3^{S253A,\ S315A}$), generating a constitutively active version of FOXO3. Expressing this version of FOXO3 in human VECs (hVECs), human VSMCs (hVSMCs), and human MSCs (hMSCs) (a stem cell component of blood vessels) improved the stress resistance properties of all of these cell types. FOXO3 activation prevented cellular aging and improved cellular resistance to oxidative stress through transcriptional suppression of *CSRP1*. Furthermore, FOXO3-enhanced human MSCs were resistant to oncogenic transformation, solving a major safety issue associated with cell transplantation therapies. Taken together, these analyses suggest that FOXO3 enhancement improves cellular homeostasis for the three types of vascular cells tested and provides a novel approach for generating safer materials for stem cell-based therapies.

RESULTS

Generation of *FOXO3*-Engineered Human Pluripotent Stem Cells

To investigate the role of FOXO3 in regulating human vascular cell homeostasis, we first evaluated FOXO3 activity in young versus senescent hMSCs, which are the major cell type within the *adventitia* of blood vessels (Chen et al., 2014; Crisan et al., 2008; Murray et al., 2014; Zengin et al., 2006; Zhang et al., 2018). FOXO3 protein levels were downregulated in replicatively senescent hMSCs (Figure 1A). In late-passage hMSCs, less nuclear FOXO3 was observed; this decrease was associated with compromised FOXO3 transcriptional activity (Figures 1B and 1C). Furthermore, FOXO3 protein levels were diminished in hMSCs derived from hESCs of Werner syndrome (a condition that drives premature aging) and physiologically aged hMSCs relative to their wild-type or young counterparts (Zhang et al., 2015; Figures 1D, S1A, and S1B; Table S1). These results establish impaired FOXO3 activity as a novel biomarker of hMSC senescence.

We next investigated whether vascular cell aging can be alleviated by FOXO3 activation. Immunofluorescence experiments indicated that alanine substitution of two of the three classical phosphorylation sites, Ser253 and Ser315 (referred to as 2SA), was sufficient to redirect FOXO3 from the cytoplasm to the nucleus, resulting in constitutive activation of FOXO3 in hMSCs (Figure S1C). Accordingly, we sought to generate homozygous $FOXO3^{2SA/2SA}$ knockin human embryonic stem cells (hESCs) using a helper-dependent adenovirus vector (HDAdV) for gene editing (Figure 1E; Liu et al., 2011, 2012, 2014; Suzuki et al., 2014; Wu et al., 2018; Yang et al., 2017). After two rounds of homologous recombination, the resultant $FOXO3^{2SA/2SA}$ hESCs exhibited common pluripotent stem cell features, including typical colony morphology, expression of the pluripotency markers, hypomethylation of the *OCT4* promoter, as well as *in vivo* differentiation into three germ layers (Figures S1D–S1F). Cell cycle kinetics and the percentage of Ki67-positive cells were both normal, indicating that the $FOXO3^{2SA/2SA}$ knockin had minimal effects on hESC proliferation (Figures S1G and S1H). Further, karyotyping and genome-wide copy number variation (CNV) analyses showed that $FOXO3^{2SA/2SA}$ hESCs were genomically stable (Figures S1I and S1J). Together, these data indicate that genetic modification of the *FOXO3* locus did not disrupt the typical features of hESCs.

FOXO3 Activation Improved Stress Resistance in Differentiated Human Vascular Endothelial and Smooth Muscle Cells

We next evaluated the effect of $FOXO3^{2SA/2SA}$ on different vascular cell types. First, $FOXO3^{+/+}$ and $FOXO3^{2SA/2SA}$ hVECs were obtained via directed differentiation of hESCs (Wu et al., 2018). $FOXO3^{+/+}$ and $FOXO3^{2SA/2SA}$ hVECs were positive for a series of endothelial cell markers, including CD31, vascular endothelial (VE)-cadherin, and von Willebrand factor (vWF) (Orlova et al., 2014; Figures 2A and S2A). $FOXO3^{2SA/2SA}$ hVECs also exhibited normal nitric oxide levels (reflecting vasodilatory properties), uptake of DiI (1,1'-dioctadecyl-3,3,3',3'-tetramethylindocarbocyanine perchlorate)-labeled acetylated low-density lipoproteins (DiI-ac-LDLs) (Figure S2B), formation of capillary-like

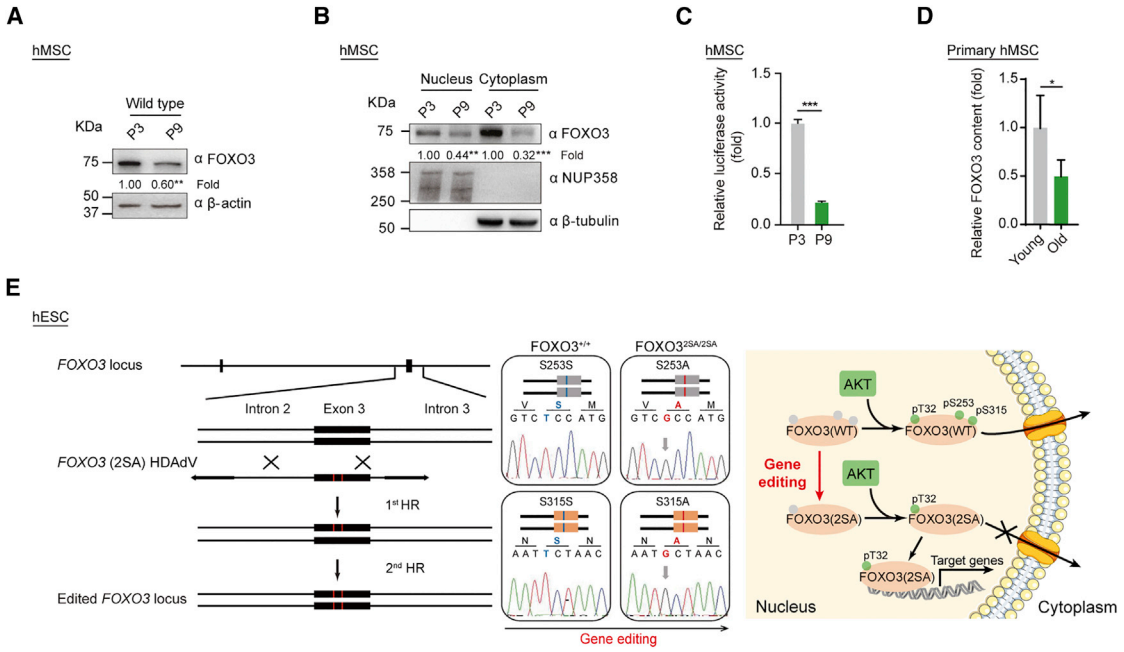

Figure 1. Generation and Characterization of *FOXO3*$^{2SA/2SA}$ hESCs

(A) Western blot analysis of the expression of FOXO3 protein in wild-type early-passage (passage 3 [P3]) and late-passage (P9) hMSCs. β-Actin was used as a loading control. The relative levels of target proteins were quantified using ImageJ software and normalized to the one in the P3 group. Data are shown as mean ± SD. n = 3, **p < 0.01 (t test).

(B) Subcellular localization of wild-type FOXO3 was analyzed by western blotting in wild-type P3 and P9 hMSCs. Nup358 was used as a loading control for nuclear protein. β-Tubulin was used as a loading control for cytoplasmic protein. The gray level of the target protein was quantified using ImageJ software and normalized to the one in the P3 group. Data are shown as mean ± SD. n = 3, **p < 0.01, ***p < 0.001 (t test).

(C) Luciferase analysis of FOXO3 transcriptional activity in wild-type P3 and P9 hMSCs using the pGL3-FHRE vector. Data are shown as mean ± SD. n = 3. ***p < 0.001 (t test). The luminescence values were normalized by the P3 group.

(D) Bar graph for the quantification of FOXO3 levels in young and old human primary MSCs. The gray levels were quantified using ImageJ software and normalized to the one in the young group. Data are shown as mean ± SD. n = 4, *p < 0.05 (t test).

(E) Schematic illustration of the *FOXO3* gene editing strategy using HDAdV. The two serines at 253 and 315 of the FOXO3 protein are replaced by alanines through two rounds of homologous recombination (HR). Red stripe, S253A and S315A. DNA sequencing demonstrates bases conversion in *FOXO3*$^{+/+}$ and *FOXO3*$^{2SA/2SA}$ hESCs. The base conversion of T757G and T943G in genomic DNA results in the change of S253A and S315A in the protein sequence, respectively. The schematic on the right shows that edited FOXO3 (FOXO3(2SA)) cannot be phosphorylated by AKT and is thus constitutively activated in the nucleus.

structures (Figure S2C), cell migration ability (Figures S2D and S2E), and comparable DNA damage levels (Figure S2F). Wild-type FOXO3 localized to the cytoplasm of hVECs, whereas activated FOXO3 primarily localized to the nuclear fraction in *FOXO3*$^{2SA/2SA}$ hVECs (Figure 2B). Consequently, *FOXO3*$^{2SA/2SA}$ hVECs exhibited moderately higher levels of cell proliferation (Figures 2C and 2D) and increased resistance to oxidative stress-induced apoptosis (Figure 2E). RNA sequencing (RNA-seq) analysis of hVECs identified 480 downregulated genes (fold change [*FOXO3*$^{+/+}$ versus *FOXO3*$^{2SA/2SA}$] > 1.5, q < 0.05) and 268 upregulated genes (fold change [*FOXO3*$^{2SA/2SA}$ versus *FOXO3*$^{+/+}$] > 1.5, q < 0.05) (Figures S2G and S2H; Table S2). Upregulated genes were enriched in genes associated with stress response pathways, consistent with the observation that FOXO3-enhanced hVECs were resistant to oxidative injury (Figures 2F, 2G, S2I, and S2J; Table S3). In line with the higher levels of cell proliferation observed for *FOXO3*$^{2SA/2SA}$ hVECs, growth-promoting genes were also upregulated in these cells (Figures 2F, 2G, and S2I).

We next differentiated *FOXO3*$^{+/+}$ and *FOXO3*$^{2SA/2SA}$ hESCs into hVSMCs. The resulting cells expressed markers specific for smooth muscles, including SM22 and Calponin (Figure 3A). *FOXO3*$^{2SA/2SA}$ hVSMCs had increased levels of nuclear FOXO3 and slightly elevated levels of cell proliferation, resembling their hVEC counterparts (Figures 3B–3D, S3A, and S3B). In addition, activation of FOXO3 protected hVSMCs from oxidative stress-induced cell apoptosis (Figures 3E and S3C–S3F; Tables S2 and S3). Transcriptomic and genomic analyses of FOXO3-enhanced hVSMCs and hVECs exhibited upregulated FOXO3 target genes (fold change > 1.5, q < 0.05) and high genomic integrity, as determined by analyzing genome-wide CNVs (Figures S3G–S3J). We subsequently evaluated the vasculogenesis activity of FOXO3-activated hVECs and hVSMCs *in vivo* using a well-established murine model of ischemia (Lian et al., 2010; Yang et al., 2017). The administration of a mixture of *FOXO3*$^{2SA/2SA}$ hVECs and hVSMCs into the mouse ischemic hindlimb muscles led to a more rapid recovery of blood flow than seen with *FOXO3*$^{+/+}$ cells (measurements were taken every 4 days after implantation) (Figures 3F and 3G). In addition, activation of FOXO3 in hVECs and hVSMCs resulted in the formation of more vessels with human antigens at

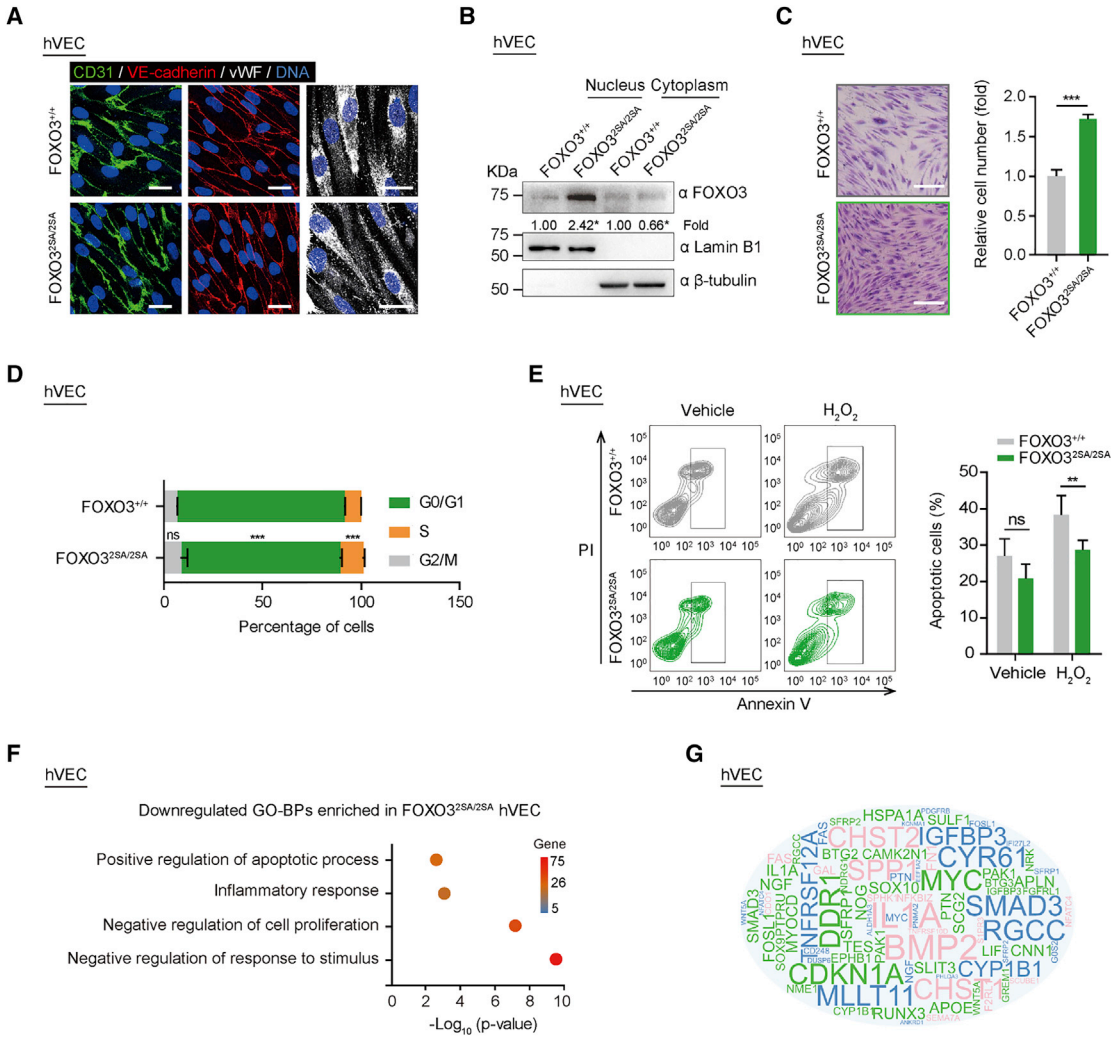

Figure 2. *FOXO3*$^{2SA/2SA}$ hVECs and hVSMCs Displayed Higher Cell Proliferation and Resistance to Oxidative Stress

(A) Immunostaining of the endothelial cell-specific markers CD31, VE-cadherin, and vWF in *FOXO3*$^{+/+}$ and *FOXO3*$^{2SA/2SA}$ hVECs. Scale bar, 25 μm.

(B) Subcellular localization of FOXO3 in *FOXO3*$^{+/+}$ and *FOXO3*$^{2SA/2SA}$ hVECs (P3), analyzed by western blotting. Lamin B1 was used as a loading control for nuclear protein. β-Tubulin was used as a loading control for cytoplasmic protein. The gray levels of target protein were quantified using ImageJ software and normalized to the ones in the *FOXO3*$^{+/+}$ group. Data are shown as mean ± SD. n = 3, *p < 0.05 (t test).

(C) Clonal expansion analysis of *FOXO3*$^{+/+}$ and *FOXO3*$^{2SA/2SA}$ hVECs at P3. The areas of crystal violet-positive cells were calculated by ImageJ. Data are shown as mean ± SD. n = 3, ***p < 0.001 (t test). Scale bar, 25 μm.

(D) Cell cycle analysis showing differential cell cycle phases in *FOXO3*$^{+/+}$ and *FOXO3*$^{2SA/2SA}$ hVECs at P3. Data are presented as mean ± SD; n = 3; ns, not significant; ***p < 0.001 (t test).

(E) Annexin V-propidium iodide (PI) staining of apoptotic *FOXO3*$^{+/+}$ and *FOXO3*$^{2SA/2SA}$ hVECs (P3) treated with 300 μM H_2O_2 for 24 hr. The percentages of apoptotic cells between *FOXO3*$^{+/+}$ and *FOXO3*$^{2SA/2SA}$ hVECs were not significantly different at the basal level (p = 0.07). Specifically, *FOXO3*$^{2SA/2SA}$ hVECs exhibited resistance to H_2O_2-induced apoptosis (p = 0.009). Data are shown as mean ± SD. n = 3, **p < 0.01 (t test).

(F) Gene ontology (GO) analysis (biological process) of downregulated genes (fold change > 1.5) in hVECs upon FOXO3 knockin (*FOXO3*$^{2SA/2SA}$ hVECs).

(G) Word cloud showing significantly downregulated genes (fold change > 1.5) in *FOXO3*$^{2SA/2SA}$ hVECs associated with negative regulation of cell proliferation (green), inflammatory response (pink), and apoptosis process (blue).

the injury sites (Figure S3K). We also observed less limb necrosis in the *FOXO3*$^{2SA/2SA}$ hVEC and hVSMC treatment group (Figure S3L). Taken together, these results indicate that the FOXO3 activation improved cellular function of hVECs and hVSMCs by increasing their self-renewal potential, making them resistant to oxidative stress, and promoting vasculature repair.

FOXO3-Activated hMSCs Were Resistant to Cellular Aging

Human MSCs localize to the *adventitia* of blood vessels and are important for maintaining blood vessel homeostasis and for repairing damage (Chen et al., 2014; Corselli et al., 2012; Crisan et al., 2008; Murray et al., 2014; Zengin et al., 2006). *FOXO3*$^{+/+}$ and *FOXO3*$^{2SA/2SA}$ hMSCs derived from hESCs both exhibited

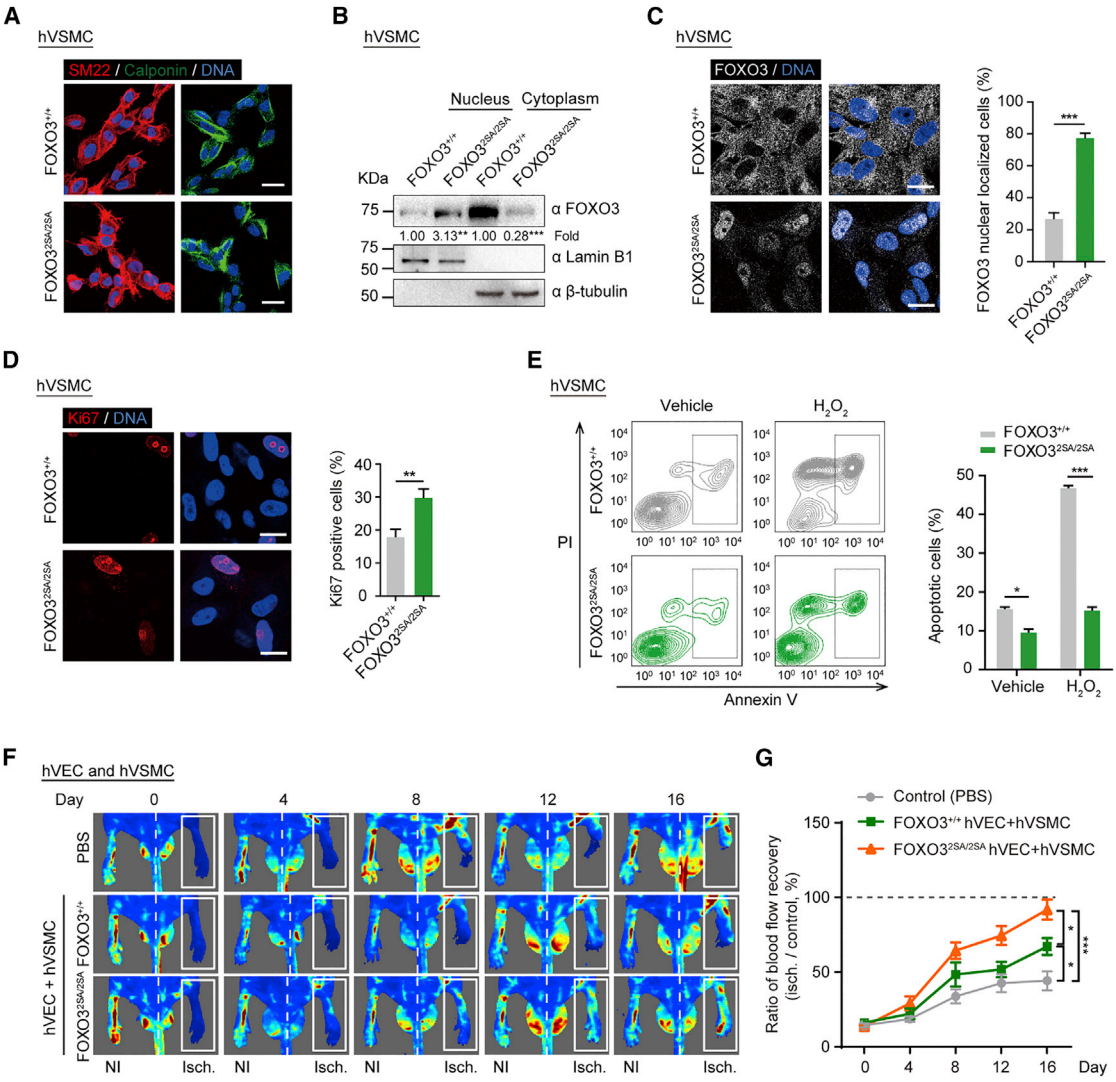

Figure 3. *FOXO3*$^{2SA/2SA}$ hVSMCs Displayed Slightly Higher Cell Proliferation and Resistance to Oxidative Stress

(A) Representative immunofluorescence micrographs of *FOXO3*$^{+/+}$ and *FOXO3*$^{2SA/2SA}$ hVSMCs exhibiting cell surface expression for the human vascular smooth muscle cell markers SM22 and Calponin. DNA was stained by Hoechst 33342. Scale bar, 25 μm.

(B) Subcellular localization of wild-type FOXO3 and *FOXO3*$^{2SA/2SA}$ protein was analyzed in *FOXO3*$^{+/+}$ and *FOXO3*$^{2SA/2SA}$ hVSMCs (P2) by western blotting. Lamin B1 was used as a loading control for nuclear protein. β-Tubulin was used as a loading control for cytoplasmic protein. The gray levels of the target protein were quantified using ImageJ software and normalized to the ones in the *FOXO3*$^{+/+}$ group. Data are shown as mean ± SD. n = 3, **p < 0.01, ***p < 0.001 (t test).

(C) FOXO3 immunofluorescence staining in *FOXO3*$^{+/+}$ and *FOXO3*$^{2SA/2SA}$ hVSMCs. Scale bar, 20 μm. Data are presented as mean ± SD. n = 6, ***p < 0.001 (t test).

(D) Ki67 immunofluorescence staining of *FOXO3*$^{+/+}$ and *FOXO3*$^{2SA/2SA}$ hVSMCs (P2). Scale bar, 20 μm. Data are presented as mean ± SD. n = 6, **p < 0.01 (t test).

(E) Annexin V-PI staining of apoptotic *FOXO3*$^{+/+}$ and *FOXO3*$^{2SA/2SA}$ hVSMCs (P2) treated with 300 μM H_2O_2 for 24 hr. Data are shown as mean ± SD. n = 3, *p < 0.05, ***p < 0.001 (t test).

(F) Representative blood flow imaging of hindlimb ischemic mice injected with PBS (control), *FOXO3*$^{+/+}$, and *FOXO3*$^{2SA/2SA}$ cells (hVECs (P3) :hVSMCs (P2) = 3:1). Laser Doppler blood perfusion measurement was performed every 4 days to monitor changes in hindlimb blood flow.

(G) Blood flow recovery kinetics of hindlimb ischemic mice after cell implantation. Statistical significance was compared between the following: *FOXO3*$^{2SA/2SA}$ group versus PBS group and *FOXO3*$^{+/+}$ group versus PBS group; *FOXO3*$^{2SA/2SA}$ group versus *FOXO3*$^{+/+}$ group. Data are presented as mean ± SEM. n = 10, *p < 0.05, ***p < 0.001 (one-way ANOVA).

features typical of mesenchymal progenitor cells, including expression of the hMSC markers CD90, CD73, and CD105 and epigenetic silencing of the *OCT4* promoter (Figures 4A, S4A, and S4B). The multi-lineage differentiation potential of *FOXO3*$^{2SA/2SA}$ hMSCs was verified using tri-lineage differentiation (Figure S4C). Genome-wide CNV analysis revealed that genomic stability was well maintained in FOXO3-enhanced hMSCs (Figure S4D). As seen with hVECs and hVSMCs, FOXO3 was present in the nuclear fraction of *FOXO3*$^{2SA/2SA}$ hMSCs (Figures 4B and S4E).

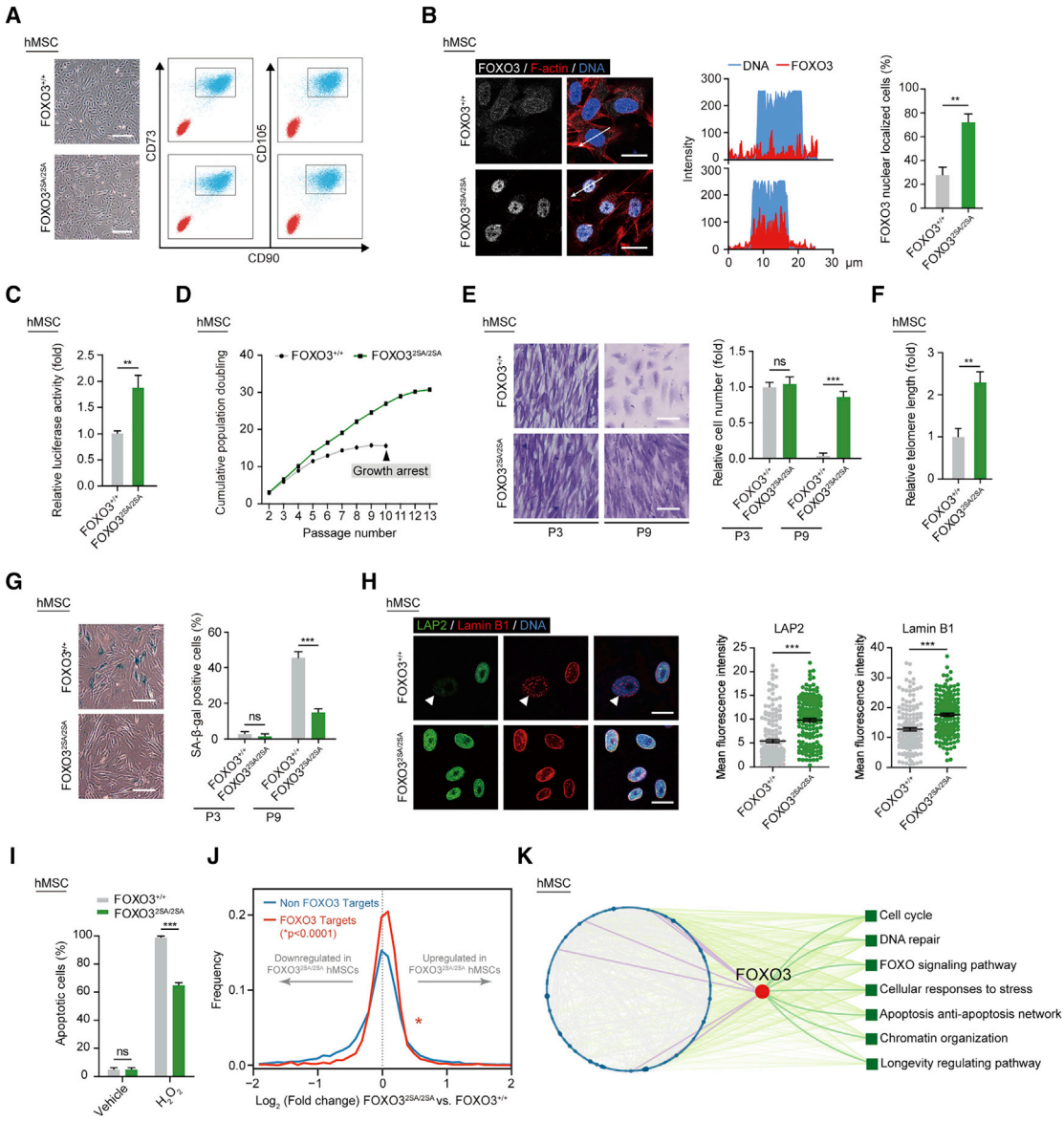

Figure 4. *FOXO3*$^{2SA/2SA}$ hMSCs Displayed Delayed Cellular Senescence

(A) Bright-field micrographs and fluorescence-activated cell sorting (FACS) analysis of the hMSCs surface markers CD73, CD90, and CD105 in *FOXO3*$^{+/+}$ and *FOXO3*$^{2SA/2SA}$ hMSCs. Scale bar, 50 μm.

(B) Representative immunostaining of FOXO3 protein in *FOXO3*$^{+/+}$ and *FOXO3*$^{2SA/2SA}$ hMSCs. Scale bar, 25 μm. The fluorescence intensities were measured by LAS AF (Leica Application Suite Advanced Fluorescence) Lite in the direction of the arrows. Most *FOXO3*$^{2SA/2SA}$ protein was expressed in the nucleus compared with wild-type FOXO3. Data are presented as mean ± SD. n = 6, **p < 0.01 (t test).

(C) Luciferase analysis of FOXO3 transcriptional activity in *FOXO3*$^{+/+}$ and *FOXO3*$^{2SA/2SA}$ hMSCs (P3) using the pGL3-FHRE vector. Data are shown as mean ± SD. n = 3, **p < 0.01 (t test).

(D) Growth curve showing the cumulative population doublings of *FOXO3*$^{+/+}$ and *FOXO3*$^{2SA/2SA}$ hMSCs over passages.

(E) Clonal expansion analysis of *FOXO3*$^{+/+}$ and *FOXO3*$^{2SA/2SA}$ hMSCs (P7). The areas of crystal violet-positive cells were calculated by ImageJ. Data are shown as mean ± SD. n = 3, ***p < 0.001 (t test). Scale bar, 50 μm.

(F) qPCR analysis of relative telomere length in *FOXO3*$^{+/+}$ and *FOXO3*$^{2SA/2SA}$ hMSCs (P7). Data are normalized to the value of the *FOXO3*$^{+/+}$ group and presented as mean ± SEM. n = 5, **p < 0.01 (t test).

(G) SA-β-gal staining analysis of *FOXO3*$^{+/+}$ and *FOXO3*$^{2SA/2SA}$ hMSCs (P7). Scale bar, 50 μm. Data are presented as mean ± SD. n = 3, ***p < 0.001 (t test).

(H) Representative immunofluorescence micrographs of LAP2 and Lamin B1 in *FOXO3*$^{+/+}$ and *FOXO3*$^{2SA/2SA}$ hMSCs (P7). White arrows denote the nuclear envelope-defective cells with decreased Lamin B1 and LAP2 expression. Scale bar, 25 μm. Quantification of mean fluorescence intensity of LAP2 and Lamin B1 in *FOXO3*$^{+/+}$ and *FOXO3*$^{2SA/2SA}$ hMSCs. Data are presented as mean ± SD, n = 8, ***p < 0.001 (t test).

(I) Annexin V-PI staining of apoptotic *FOXO3*$^{+/+}$ and *FOXO3*$^{2SA/2SA}$ hMSCs (P7) treated with 500 μM H_2O_2 for 24 hr. Data are presented as mean ± SD. n = 3, ***p < 0.001 (t test).

(legend continued on next page)

Next we investigated the effect of FOXO3 activation on hMSC homeostasis. Reporter assays verified an increase in FOXO3 transcriptional activity in genetically edited cells (Figure 4C). Compared with *FOXO3*$^{+/+}$ hMSCs, *FOXO3*$^{2SA/2SA}$ hMSCs consistently exhibited decreased senescence-associated (SA) β-galactosidase (β-gal) activity, increased cell proliferation, elongated telomeres, and reduced reactive oxygen species (ROS) levels (Figures 4D–4G, S4F, and S4G). They also showed improved nuclear and chromosomal architecture and less activation of DNA damage responses (Figures 4H and S4H–S4K; Tables S2 and S3; López-Otín et al., 2013; Zhang et al., 2015). Moreover, FOXO3 activation rendered MSCs refractory to H_2O_2-induced cellular apoptosis (Figure 4I). Transcriptomic analyses indicated that genetic activation of FOXO3 upregulated 32 known FOXO3 target genes (fold change > 1.5, q < 0.05) (Figure 4J, S4L, and S4M). Although, in WT MSCs, replicative stress resulted in downregulation of genes associated with the maintenance of chromosome organization, cell cycle progression, DNA repair, and stress resistance, FOXO3-enhanced MSCs were less sensitive to replicative senescence-associated gene expression changes (Figures 4K and S4N–S4S; Table S4). Taken together, these results indicate that FOXO3 activation improved the fitness of hMSCs.

Finally, we tested whether FOXO3 activation alleviated cellular senescence in the context of Werner syndrome (WS), a premature aging disorder (Geng et al., 2018; Zhang et al., 2015). FOXO3-enhanced, WS-specific hMSCs (*FOXO3*$^{2SA/2SA}$ *WRN*$^{-/-}$ hMSCs) were generated using a combination of gene editing and hESC-directed differentiation procedures (Figures S4T and S4U). As expected, FOXO3 activation improved self-renewal activity and reduced aging hallmarks in *WRN*$^{-/-}$ hMSCs (Figures S4V–S4Y), further indicating that FOXO3 activation was capable of delaying hMSCs senescence, even in the context of pathological aging.

FOXO3 Activation Improved Vascular Cell Functionality via *trans* Suppression of *CSRP1* Expression

To understand the molecular mechanism by which FOXO3 activation improved the functionality of vascular cells, we analyzed the effect of FOXO3 activation on gene expression in hVECs, hVSMCs, and hMSCs (Figures S5A–S5G). When gene expression changes were compared between cell types, 9 upregulated genes and 34 downregulated genes were shared among all three cell types (Figure S5A). Cysteine- and glycine-rich protein 1 (CSRP1), a cysteine-rich protein (CRP) family member involved in a wide range of biological processes (Latonen et al., 2010; Pomiès et al., 1997; Schmeichel and Beckerle, 1998), was the most significantly downregulated gene across *FOXO3*$^{2SA/2SA}$ hVECs, hVSMCs, and hMSCs (Figures S5A–S5D). In line with this RNA-seq result, CSRP1 protein was undetectable in *FOXO3*$^{2SA/2SA}$ hVECs, hVSMCs, and hMSCs relative to WT cells (Figure 5A). We next cloned the *CSRP1* promoter upstream of a luciferase reporter. Diminished *CSRP1* promoter activity was observed in *FOXO3*$^{2SA/2SA}$ hMSCs compared with WT controls (Figure 5B). A potential FOXO3 binding site was predicted within the *CSRP1* promoter. Mutation of a single nucleotide (ACG to CCG) within this predicted binding site prevented activated FOXO3 from inhibiting *CSRP1* transcription (Figure 5B). Using chromatin immunoprecipitation (ChIP)-qPCR, we further found enrichment of FOXO3 at the *CSRP1* promoter specifically in *FOXO3*$^{2SA/2SA}$ hMSCs (Figure 5C). This was coupled with enhanced recruitment of the deacetylase SIRT1 as well as decreased levels of the SIRT1 substrate H3K9ac an active histone mark (Figures 5D and 5E). Overexpression of SIRT1 in WT or *FOXO3*$^{2SA/2SA}$ hMSCs repressed *CSRP1* promoter activity (Figure 5F), supporting an inhibitory role of SIRT1 recruitment in *CSRP1* expression (Figure 5G). Additionally, we observed DNA hypermethylation and reduced levels of the active histone mark H3K4me3 at the *CSRP1* promoter (Figures 5E and 5H). These results were consistent with activated FOXO3 creating a repressive chromatin environment at the *CSRP1* promoter, partially by recruiting SIRT1, resulting in *CSRP1* silencing (Figures 5H, S5H, and S5I). Collectively, these data reveal that activated FOXO3 functions as a transcriptional repressor of *CSRP1* in human vascular cells.

To determine whether downregulation of CSRP1 in *FOXO3*$^{2SA/2SA}$ hMSCs exerted cytoprotective effects, we re-introduced CSRP1 into *FOXO3*$^{2SA/2SA}$ hMSCs using lentiviral vector-mediated gene transfer (Figure S6A). Re-expression of CSRP1 restored cellular aging features, including impaired cell proliferation, increased SA β-gal activity, upregulation of p16, p21, and inflammatory factors, as well as loss of Lamin B1 (Figures 6A–6C). RNA-seq analysis revealed that restoration of CSRP1 in *FOXO3*$^{2SA/2SA}$ hMSCs resulted in a gene expression profile resembling that seen with *FOXO3*$^{+/+}$ cells (Figure 6D, S6B, and S6C; Table S2). In contrast, knockdown of CSRP1 in *FOXO3*$^{+/+}$ hMSCs alleviated various signatures of cellular aging (Figures S6D–S6H). We also confirmed that downregulation of CSRP1 was important for the beneficial effect in *FOXO3*$^{2SA/2SA}$ hVEC and hVSMCs (Figures 6E, 6F, and S6I–S6K). Together, these results indicate that *FOXO3*$^{2SA/2SA}$-mediated CSRP1 suppression contributed to the protective effects in various *FOXO3*-engineered vascular cells.

FOXO3-Enhanced hMSCs Exhibited a Superior Therapeutic Effect on Vascular Degeneration

Accumulating evidence indicates that hMSCs can be used to promote vasculature regeneration in the context of aging and vascular injuries (de Souza et al., 2016; Yang et al., 2017). We therefore used a murine model of ischemia to find out whether *FOXO3*$^{2SA/2SA}$ hMSCs could improve therapeutic outcomes *in vivo* (Lian et al., 2010). Injection of *FOXO3*$^{2SA/2SA}$ hMSCs into ischemic hindlimb muscles resulted in a more rapid recovery of blood flow than seen with *FOXO3*$^{+/+}$ cells (Figures 7A and 7B).

(J) Polygon frequency graph of Log_2 mRNA expression fold changes of *FOXO3* target genes between *FOXO3*$^{+/+}$ and *FOXO3*$^{2SA/2SA}$ hMSCs (P3). A rightward shift of the *FOXO3* target plot indicates that part of the *FOXO3* target genes were upregulated in *FOXO3*$^{2SA/2SA}$ hMSCs (two-sample Kolmogorov-Smirnov test, $p = 2.2 \times 10^{-16}$).

(K) NAViGaTOR visualization of protein-protein interaction (PPI) functional interaction network analysis of upregulated genes (fold change > 1.5) in *FOXO3*$^{2SA/2SA}$ hMSCs (P7) with the Integrated Interactions Database (IID). Node color indicates the fold change of the upregulated genes, and node size indicates the interaction numbers with the other nodes. Right: selected representative pathways identified using pathDIP.

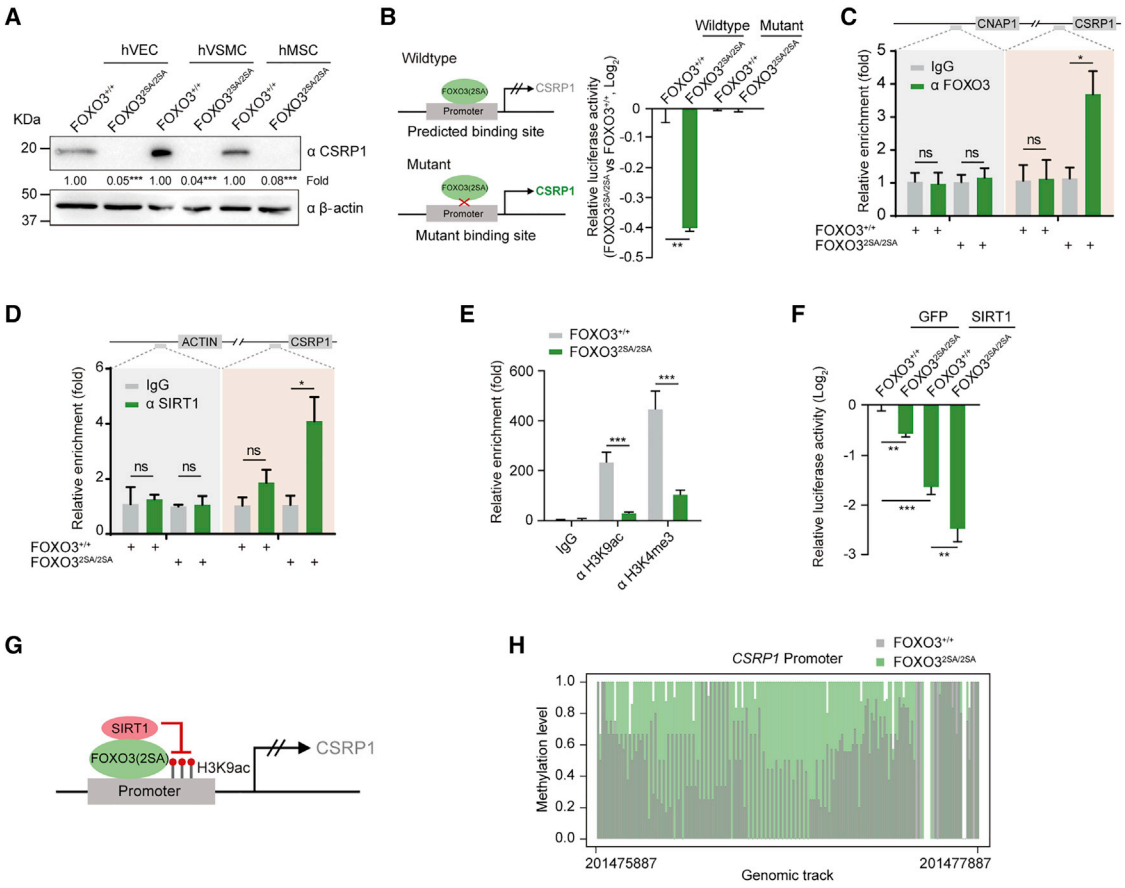

Figure 5. Identification of *CSRP1* as a Target Gene of FOXO3$^{2SA/2SA}$

(A) Western blot analysis of CSRP1 protein in *FOXO3*$^{+/+}$ and *FOXO3*$^{2SA/2SA}$ hVECs (P3), hVSMCs (P2), and hMSCs (P3). β-Actin was used as the loading control. The gray levels of target protein were quantified using ImageJ software and normalized to the ones in the *FOXO3*$^{+/+}$ group. Data are shown as mean ± SD. n = 3, ***p < 0.001 (t test).

(B) Transcriptional activity of FOXO3 in *FOXO3*$^{+/+}$ and *FOXO3*$^{2SA/2SA}$ hMSCs measured by dual luciferase reporter assay. *FOXO3*$^{+/+}$ and *FOXO3*$^{2SA/2SA}$ hMSCs were transfected with the pGL3-CSRP1 promoter (wild-type; predicted binding site, GGAAAACG), pGL3-CSRP1 promoter (mutant; mutant binding site, GGAAACCG) and *Renilla* plasmid. Data are presented as mean ± SD. n = 3, ***p < 0.001 (t test).

(C) ChIP-qPCR analysis of the occupancy of FOXO3 on the *CSRP1* promoter and negative control regions in hMSCs using an anti-FOXO3 antibody. The diagram above depicts the relative position of primer pairs used for ChIP-qPCR. Exons are depicted as gray boxes. Data are presented as mean ± SEM. n = 6, **p < 0.01 (t test).

(D) ChIP-qPCR analysis of the occupancy of SIRT1 on the *CSRP1* promoter and negative control regions in hMSCs using an anti-SIRT1 antibody. The diagram above depicts the relative position of primer pairs used for ChIP-qPCR. Exons are depicted as gray boxes. Data are presented as mean ± SEM. n = 6, *p < 0.05 (t test).

(E) ChIP-qPCR analysis of the occupancy of H3K9ac and H3K4me3 on the *CSRP1* promoter region in hMSCs. Data are presented as mean ± SEM. n = 6, ***p < 0.001 (t test).

(F) Transcriptional activity of FOXO3 in *FOXO3*$^{+/+}$ and *FOXO3*$^{2SA/2SA}$ hMSCs transfected with GFP or SIRT1, measured by dual luciferase reporter assay. Data are presented as mean ± SD. n = 3, **p < 0.01, ***p < 0.001 (t test).

(G) Schematic plot showing that enhanced recruitment of SIRT1 at the *CSRP1* promoter in *FOXO3*$^{2SA/2SA}$ hMSCs decreased the H3K9ac level and repressed the transcription of *CSRP1*.

(H) DNA methylation boxplot of *CSRP1* promoter in *FOXO3*$^{+/+}$ and *FOXO3*$^{2SA/2SA}$ hMSCs. Dots indicate the unmethylated and methylated CpG sites. The color and height of the bars represent the sample and DNA methylation levels, respectively.

As a control, administration of primary hMSCs had similar results as administration of *FOXO3*$^{+/+}$ hMSCs (Figures 7A and 7B). Analysis of human antigen specific for hVECs (hCD31) revealed the appearance of more human vascular cells in muscles that received *FOXO3*$^{2SA/2SA}$ hMSCs relative to those implanted with *FOXO3*$^{+/+}$ or primary hMSCs (Figures 7C and S7A). Consistently, less limb necrosis was observed in the *FOXO3*$^{2SA/2SA}$ hMSC treatment group (Figure S7B). Together, these results indicate that FOXO3-engineered hMSCs had enhanced vascular regeneration potential under pathological conditions such as limb ischemia.

FOXO3-Activated hMSCs Were Resistant to Oncogenic Transformation

Given that FOXO3 is a potent tumor suppressor (Dansen and Burgering, 2008; Medema et al., 2000), we hypothesized that hMSCs

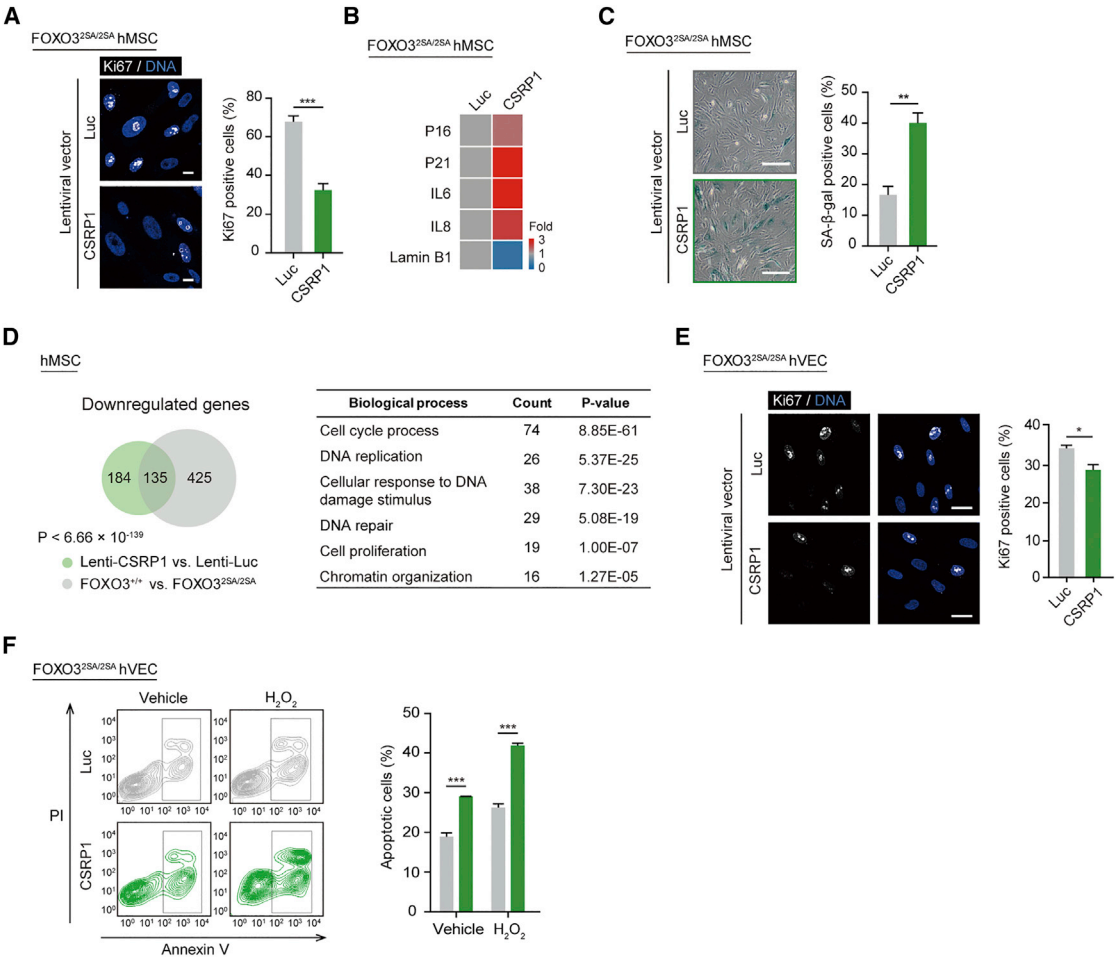

Figure 6. *CSRP1* Mediated the Protective Effect of FOXO3 Enhancement on Human Vascular Cells

(A) Ki67 immunofluorescence staining of *FOXO3*$^{2SA/2SA}$ hMSCs expressing Luc or CSRP1. Scale bar, 50 μm. Data are presented as mean ± SD. n = 6, ***p < 0.001 (t test).

(B) qRT-PCR analysis of the expression of aging-related markers (P16, P21, interleukin-6 [IL-6], IL-8, and Lamin B1) in *FOXO3*$^{2SA/2SA}$ hMSCs expressing Luc or CSRP1. n = 4, *p < 0.05 (t test).

(C) SA-β-gal staining of *FOXO3*$^{2SA/2SA}$ hMSCs expressing Luc or CSRP1. Scale bar, 50 μm. Data are presented as mean ± SD, n = 4, **p < 0.01 (t test).

(D) Left: Venn diagram showing genes commonly downregulated in both *FOXO3*$^{+/+}$ hMSC (compared to *FOXO3*$^{2SA/2SA}$ hMSC at P7) and CSRP1-OE hMSCs (compared to Luc-OE *FOXO3*$^{2SA/2SA}$ hMSCs). Right: GO analysis (biological process) of 135 overlapped genes between CSRP1-overexpressing and *FOXO3*$^{+/+}$ hMSCs (P7) (hypergeometric test, p = 6.66 × 10^{-139}). OE: overexpressed.

(E) Ki67 immunofluorescence staining of *FOXO3*$^{2SA/2SA}$ hVECs expressing Luc or CSRP1. Scale bar, 50 μm. Data are presented as mean ± SD, n = 6, *p < 0.05 (t test).

(F) Annexin V-PI staining of apoptotic Luc- or CSRP1-transduced *FOXO3*$^{+/+}$ and *FOXO3*$^{2SA/2SA}$ hVECs treated with 300 μM H_2O_2 for 24 hr, respectively. Data are shown as mean ± SD. n = 3, ***p < 0.001 (t test).

expressing constitutively activated FOXO3 would be resistant to oncogenic transformation. RNA-seq analysis demonstrated that a panel of genes with tumor-suppressing activities were upregulated in *FOXO3*$^{2SA/2SA}$ hMSCs relative to their WT counterparts (Figure 7D). When *FOXO3*$^{2SA/2SA}$ hMSCs were implanted into immunodeficient mice, no tumors were evident 6 months after the engraftment procedure (Figure S7C). We further asked whether *FOXO3*$^{2SA/2SA}$ hMSCs could be transformed in the presence of oncogenic insults. *FOXO3*$^{+/+}$ and *FOXO3*$^{2SA/2SA}$ hMSCs were transduced sequentially with lentiviral or retroviral vectors expressing *hTERT*, *SV40 T* antigens, short hairpin RNA (shRNA)-*p53*, and *hRasV12* (we refer to these transformed MSCs as hTMSCs) (Figures 7E and S7D; Scaffidi and Misteli, 2011). Although both *FOXO3*$^{+/+}$ and *FOXO3*$^{2SA/2SA}$ hTMSCs exhibited replicative immortality (Figure S7E), *FOXO3*$^{2SA/2SA}$ hTMSCs formed fewer and smaller colonies in soft agarose, indicating suppressed tumorigenic potential (Figure 7F). We next investigated the *in vivo* tumorigenicity of *FOXO3*$^{+/+}$ and *FOXO3*$^{2SA/2SA}$ hTMSCs by implanting them into the tibia (proximal to the knee joint) of immunodeficient mice. Only *FOXO3*$^{+/+}$ hTMSCs (6 of 6 compared with 0 of 6 in *FOXO3*$^{2SA/2SA}$ cells) developed into solid tumors within 4 months of engraftment (Figure 7G). These data indicate that FOXO3 activation protected against tumorigenic transformation when cells were confronted with oncogenic insults.

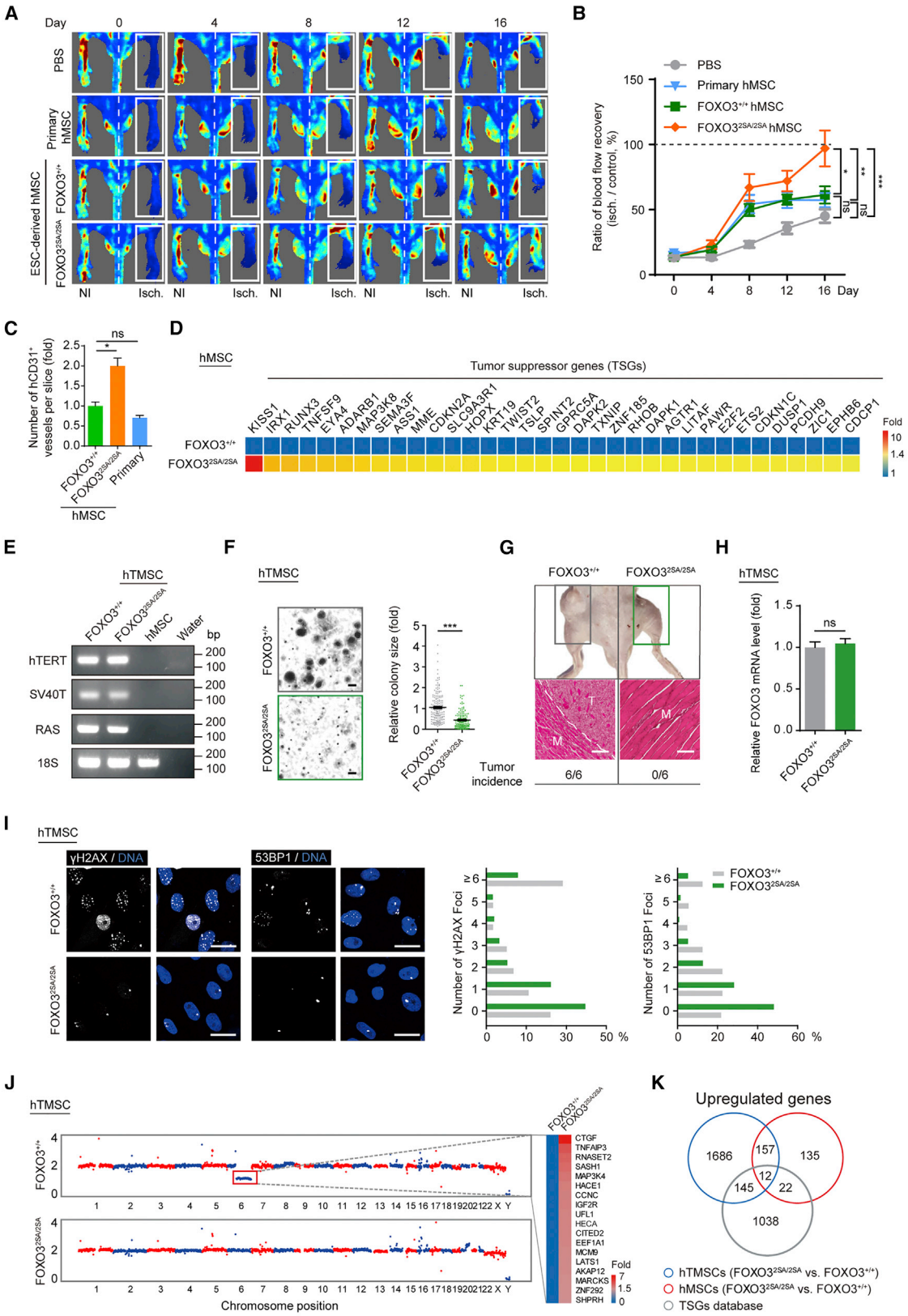

(legend on next page)

To gain further insight into the molecular signatures associated with transformation resistance of FOXO3-enhanced hMSCs, we analyzed the transcriptional and genome landscapes in *FOXO3*$^{+/+}$ and *FOXO3*$^{2SA/2SA}$ hTMSCs. Although *FOXO3*$^{+/+}$ hTMSCs exhibited global genomic instability, as indicated by substantial CNV and increased intranuclear foci of γH2AX and 53BP1, FOXO3 activation safeguarded genomic integrity in *FOXO3*$^{2SA/2SA}$ hTMSCs (Figures 7H–7J). RNA-seq analysis showed that, in *FOXO3*$^{2SA/2SA}$ hTMSCs, genes involved in cell division were downregulated, whereas genes involved in tumor suppression were upregulated (Figures S7F and S7G; Tables S2 and S3). According to the Tumor Suppressor Gene (TSG) database, 157 TSGs were upregulated in *FOXO3*$^{2SA/2SA}$ hTMSCs, which may account for the associated tumor-repressive potential (Figure 7K). Collectively, these data indicate that FOXO3 activation in hMSCs rendered these cells resistant to oncogenic transformation by, at least in part, safeguarding genomic stability and transcriptionally inducing tumor suppressor genes.

DISCUSSION

Vascular aging results in the functional decline and structural alteration of blood vessel endothelial cells, VSMCs, and pericytes (also considered MSCs; Chen et al., 2014; Corselli et al., 2012; Crisan et al., 2008). These changes are correlated with disrupted organismal homeostasis and a shortened lifespan (Laina et al., 2018; Regina et al., 2016). Studies of centenarians revealed that FOXO3 is the most conserved longevity gene; the presence of certain FOXO3 alleles correlates with human longevity. Here, using genome editing technology, we recoded two Akt phosphorylation sites within the FOXO3 protein, generating a constitutively active version. We then showed that activated FOXO3 improved vascular homeostasis. Major conclusions from these studies were as follows: FOXO3 activity was compromised in physiologically and pathologically aged hMSCs; FOXO3-enhanced hVECs, hVSMCs, and hMSCs exhibited improved self-renewal and increased resistance to oxidative injury; constitutive FOXO3 activation alleviated physiological and premature hMSC senescence; FOXO3-engineered hVECs, hVSMCs, and hMSCs promoted greater regenerative repair *in vivo* under ischemia conditions; and genetic enhancement in FOXO3 rendered hMSCs resistant to oncogenic transformation. For the first time, we showed that genetically activated FOXO3 contributes to the maintenance of vascular homeostasis, providing a novel strategy for generating stem cells that are more effective and safer when used for regenerative therapies.

It has been shown previously that FOXO3 is important for maintaining cardiovascular homeostasis and preventing cardiovascular aging (Martins et al., 2016; Paik, 2006). For example, FOXO3-deficient mice develop dilated cardiomyopathy within 12 weeks of age (Ni et al., 2006). In contrast, FOXO3 nuclear activation promotes the survival of HUVECs and astrocytes under oxidative stress conditions (Fluteau et al., 2015). To date, it is still unknown whether a genetic variation to the human *FOXO3* gene is causally linked to enhanced vascular cell activity. Our study presents the first evidence that genetic modification of two nucleotides in the human *FOXO3* gene is sufficient to cause nuclear accumulation of FOXO3 and substantial improvements in multiple aspects of vascular functions. These findings provide a promising new avenue for strengthening cardiovascular health in humans.

In addition to functioning as a transcriptional activator, FOXO3 also *trans*-represses certain gene promoters. For example, FOXO3 binding to the *Skp2* promoter inhibits *Skp2* expression and prevents tumorigenesis (Wu et al., 2013). In addition, activated FOXO3 suppresses the expression of MYC target genes by associating with their promoters (Bouchard et al., 2004). We showed, for the first time, that constitutively activated FOXO3 can act as a transcriptional repressor in three types of human vascular cells. Binding of activated FOXO3 to the *CSRP1* promoter helped recruit the histone deacetylase SIRT1, resulting in H3K9 deacetylation and *CSRP1* silencing. We further demonstrated that CSRP1 counteracted cell proliferation and survival and that downregulation of CSRP1 mediated the major benefits derived from FOXO3 activation. Therefore, the FOXO3-CSRP1 axis may represent a new target for vasculoprotection.

Concerning the clinical relevance of these findings, MSCs are regarded as one of the most useful stem cell types in cell replacement therapies (Keating, 2012; Resnick et al., 2013; Trounson and McDonald, 2015). MSCs have been utilized in

Figure 7. *FOXO3*$^{2SA/2SA}$ hMSCs Promoted Revascularization and Were Resistant to Oncogene-Induced Neoplastic Transformation

(A) Representative blood flow imaging of hindlimb ischemic mice injected with PBS (control), *FOXO3*$^{+/+}$, *FOXO3*$^{2SA/2SA}$ hMSCs (P8), and primary MSCs (P7). Laser Doppler blood perfusion measurement was performed every 4 days to monitor changes in hindlimb blood flow.

(B) Blood flow recovery kinetics of hindlimb ischemic mice after cell implantation. Statistical significance was compared between the following: *FOXO3*$^{2SA/2SA}$ group versus PBS group; *FOXO3*$^{+/+}$ group versus PBS group; primary MSC group versus PBS group; *FOXO3*$^{2SA/2SA}$ group versus *FOXO3*$^{+/+}$ group; *FOXO3*$^{2SA/2SA}$ group versus primary MSC group. Data are presented as mean ± SEM. n = 6, *p < 0.05, **p < 0.01, ***p < 0.001 (one-way ANOVA).

(C) Bar graph showing the normalized number of vessels per slice in ischemic hindlimbs injected with *FOXO3*$^{+/+}$, *FOXO3*$^{2SA/2SA}$ hMSCs (P8), and primary hMSCs (P7). Data are presented as mean ± SD, n = 6, *p < 0.05 (t test).

(D) Heatmap showing the expression of tumor suppressor genes in *FOXO3*$^{+/+}$ and *FOXO3*$^{2SA/2SA}$ hMSCs at P3.

(E) RT-PCR analysis of the levels of indicated oncogenic transformation factors in *FOXO3*$^{+/+}$ and *FOXO3*$^{2SA/2SA}$ hTMSCs. Untransformed *FOXO3*$^{+/+}$ hMSCs were used as a negative control.

(F) Soft agar assay analysis of the anchorage-independent growth ability of *FOXO3*$^{+/+}$ and *FOXO3*$^{2SA/2SA}$ hTMSCs (P7) *in vitro*. Scale bar, 50 μm.

(G) Representative images of the *in vivo* tumor formation ability of hTMSCs. *FOXO3*$^{+/+}$ and *FOXO3*$^{2SA/2SA}$ hTMSCs (P7) were implanted into the left or right upper tibia of immunodeficient mice, respectively. Scale bar, 100 μm.

(H) qRT-PCR analysis of the levels of FOXO3 transcripts in *FOXO3*$^{+/+}$ and *FOXO3*$^{2SA/2SA}$ hTMSCs (P7). Data are presented as mean ± SEM, n = 4.

(I) Representative immunofluorescence images of DNA damage markers in *FOXO3*$^{+/+}$ and *FOXO3*$^{2SA/2SA}$ hTMSCs (P7). Scale bar, 25 μm. The numbers of γH2AX and 53BP1 foci in the nuclei of *FOXO3*$^{+/+}$ and *FOXO3*$^{2SA/2SA}$ hTMSCs were quantified.

(J) Whole-genome analysis of copy number variations (CNVs) in *FOXO3*$^{+/+}$ and *FOXO3*$^{2SA/2SA}$ hTMSCs by deep sequencing. Tumor-promoting genes in the loss region of chromosome 6 are as indicated.

(K) Venn diagram showing the numbers of upregulated tumor suppressor genes among *FOXO3*$^{2SA/2SA}$ hMSCs, hTMSCs, and tumor suppressor genes (TSGs).

several preclinical studies and early-phase clinical trials (phase I, I/II, or II) (Squillaro et al., 2016). Administrating MSCs to patients with ischemic stroke or neurodegenerative disease consistently promotes functional recovery and tissue regeneration (Joyce et al., 2010). Nevertheless, therapeutic efficiency and safety concerns remain major challenges for these preclinical and clinical applications (Hentze et al., 2007; Wang et al., 2012). FOXO3 is viewed as a *bona fide* cell protector and tumor suppressor. Our study demonstrated that FOXO3-activated hVECs, hVSMCs, and hMSCs all promoted blood flow recovery following an ischemic injury, suggesting that this type of strategy could be used to treat diverse disorders related to vascular degeneration. In terms of clinical safety, activating FOXO3 abrogates the *in vivo* tumor-forming ability of human stem cells. Furthermore, given that hESC-derived hMSCs or other lineage derivatives represent inexhaustible resources for cell replacement therapies and that FOXO3 plays protective roles in numerous tissues of our body, it is reasonable to speculate that *FOXO3* genetically enhanced human (stem or progenitor) cells could be part of a wide range of therapeutic interventions well beyond those described here.

In conclusion, our findings provide novel mechanistic insights into FOXO3-mediated vascular protection and reveal FOXO3 activation as a novel strategy for generating more effective and safe biomaterials for cell replacement therapy.

STAR★METHODS

Detailed methods are provided in the online version of this paper and include the following:

SUPPLEMENTAL INFORMATION

Supplemental Information includes seven figures and five tables and can be found with this article online at https://doi.org/10.1016/j.stem.2018.12.002.

ACKNOWLEDGMENTS

The authors acknowledge L. Bai, R. Bai, M. Wei, Q. Chu, J. Lu, and S. Ma for administrative assistance; M. Wei, X. Zhang, and J. Jia for assisting with animal experiments; J. Jia and S. Sun for help with FACS; X. Shi, X. Wu, M. Wang, S. Yang, S. Duo, K. Du, and L. Zhou for management of laboratory animals; C. Peng for TEM sample preparation; D. Lv for muscle biopsy; and X.X. and J.Y. for preliminary testing and technical assistance. We thank all members of the Liu lab for discussions and technical support. This work was supported by the National Key Research and Development Program of China (2018YFC2000100), the Strategic Priority Research Program of the Chinese Academy of Sciences (XDA16010100), the National Key Research and Development Program of China (2015CB964800, 2018YFA0107203, 2017YFA0103304, 2017YFA0102802, and 2014CB910503), the National Natural Science Foundation of China, China (81422017, 81625009, 81330008, 91749202, 91749123, 31671429, 81671377, 81771515, 31601109, 31601158, 81701388, 81601233, 81471414, 81870228, 81822018, 81801399, 31801010, 81801370, and 81861168034), Program of Beijing Municipal Science and Technology Commission (Z151100003915072), Key Research Program of the Chinese Academy of Sciences (KJZDEWTZ-L05), Beijing Municipal Commission of Health and Family Planning (PXM2018_026283_000002), Advanced Innovation Center for Human Brain Protection (117212), and the State Key Laboratory of Membrane Biology, China. K.S. was supported by Takeda Science Foundation, Japan. J.C.I.B. was supported by the G. Harold and Leila Y. Mathers Charitable Foundation, United States, The Moxie Foundation, and The Glenn Foundation. Some of the bioinformatics analyses were performed on the High Performance Computing Platform of the Center for Life Science.

AUTHOR CONTRIBUTIONS

G.-H.L., F.T., and J.Q. conceptualized the work and supervised the overall experiments. P.Y. and L.W. performed the phenotypic and mechanistic analyses. J.Q. and K.S. generated gene-edited human embryonic stem cells. Q.L. and P.L. performed bioinformatics analyses. W.Z., Z.L., X.H., and S.W. guided cell culture, differentiation, and data analysis; P.Y., L.W., and Q.L. performed molecular experiments. P.Y., L.W., J.L., and W.L. performed animal experiments. P.Y. performed plasmid construction. J.D. isolated primary human MSCs. P.C. performed data analysis. G.-H.L., F.T., J.Q., W.Z., M.S., J.C.I.B., P.Y., and Q.L. performed data analysis and wrote the manuscript. All authors reviewed the manuscript.

DECLARATION OF INTERESTS

The authors declare no competing interests

Received: June 19, 2018
Revised: October 29, 2018
Accepted: December 5, 2018
Published: January 17, 2019

REFERENCES

Anders, S., Pyl, P.T., and Huber, W. (2015). HTSeq–a Python framework to work with high-throughput sequencing data. Bioinformatics *31*, 166–169.

Azene, N., Fu, Y., Maurer, J., and Kraitchman, D.L. (2014). Tracking of stem cells in vivo for cardiovascular applications. J. Cardiovasc. Magn. Reson. *16*, 7.

Bouchard, C., Marquardt, J., Brás, A., Medema, R.H., and Eilers, M. (2004). Myc-induced proliferation and transformation require Akt-mediated phosphorylation of FoxO proteins. EMBO J. *23*, 2830–2840.

Brown, K.R., Otasek, D., Ali, M., McGuffin, M.J., Xie, W., Devani, B., Toch, I.L., and Jurisica, I. (2009). NAViGaTOR: Network Analysis, Visualization and Graphing Toronto. Bioinformatics *25*, 3327–3329.

Brunet, A., Bonni, A., Zigmond, M.J., Lin, M.Z., Juo, P., Hu, L.S., Anderson, M.J., Arden, K.C., Blenis, J., and Greenberg, M.E. (1999). Akt promotes cell survival by phosphorylating and inhibiting a Forkhead transcription factor. Cell *96*, 857–868.

Brunet, A., Sweeney, L.B., Sturgill, J.F., Chua, K.F., Greer, P.L., Lin, Y., Tran, H., Ross, S.E., Mostoslavsky, R., Cohen, H.Y., et al. (2004). Stress-dependent regulation of FOXO transcription factors by the SIRT1 deacetylase. Science *303*, 2011–2015.

Chen, W.C., Saparov, A., Corselli, M., Crisan, M., Zheng, B., Péault, B., and Huard, J. (2014). Isolation of blood-vessel-derived multipotent precursors from human skeletal muscle. J. Vis. Exp. *90*, e51195.

Cho, S.W., Moon, S.H., Lee, S.H., Kang, S.W., Kim, J., Lim, J.M., Kim, H.S., Kim, B.S., and Chung, H.M. (2007). Improvement of postnatal neovascularization by human embryonic stem cell derived endothelial-like cell transplantation in a mouse model of hindlimb ischemia. Circulation *116*, 2409–2419.

Chung, W.H., Dao, R.L., Chen, L.K., and Hung, S.I. (2010). The role of genetic variants in human longevity. Ageing Res. Rev. *9* (*Suppl 1*), S67–S78.

Clark, S.J., Smallwood, S.A., Lee, H.J., Krueger, F., Reik, W., and Kelsey, G. (2017). Genome-wide base-resolution mapping of DNA methylation in single cells using single-cell bisulfite sequencing (scBS-seq). Nat. Protoc. *12*, 534–547.

Cole, T., Williams, B.A., Geo, P., Ali, M., Gordon, K., Baren, M.J., Van, Salzberg, S.L., Wold, B.J., and Lior, P. (2010). Transcript assembly and quantification by RNA-Seq reveals unannotated transcripts and isoform switching during cell differentiation. Nature Biotechnology *28*, 511–515.

Corselli, M., Chen, C.W., Sun, B., Yap, S., Rubin, J.P., and Péault, B. (2012). The tunica adventitia of human arteries and veins as a source of mesenchymal stem cells. Stem Cells Dev. *21*, 1299–1308.

Counter, C.M., Hahn, W.C., Wei, W., Caddle, S.D., Beijersbergen, R.L., Lansdorp, P.M., Sedivy, J.M., and Weinberg, R.A. (1998). Dissociation among in vitro telomerase activity, telomere maintenance, and cellular immortalization. Proc. Natl. Acad. Sci. USA *95*, 14723–14728.

Crisan, M., Yap, S., Casteilla, L., Chen, C.W., Corselli, M., Park, T.S., Andriolo, G., Sun, B., Zheng, B., Zhang, L., et al. (2008). A perivascular origin for mesenchymal stem cells in multiple human organs. Cell Stem Cell *3*, 301–313.

Dansen, T.B., and Burgering, B.M. (2008). Unravelling the tumor-suppressive functions of FOXO proteins. Trends Cell Biol. *18*, 421–429.

Datsenko, K.A., and Wanner, B.L. (2000). One-step inactivation of chromosomal genes in Escherichia coli K-12 using PCR products. Proc. Natl. Acad. Sci. USA *97*, 6640–6645.

de Souza, L.E., Malta, T.M., Kashima Haddad, S., and Covas, D.T. (2016). Mesenchymal stem cells and pericytes: to what extent are they related? Stem Cells Dev. *25*, 1843–1852.

Deng, L., Huang, L., Sun, Y., Heath, J.M., Wu, H., and Chen, Y. (2015). Inhibition of FOXO1/3 promotes vascular calcification. Arterioscler. Thromb. Vasc. Biol. *35*, 175–183.

Duan, S., Yuan, G., Liu, X., Ren, R., Li, J., Zhang, W., Wu, J., Xu, X., Fu, L., Li, Y., et al. (2015). PTEN deficiency reprogrammes human neural stem cells towards a glioblastoma stem cell-like phenotype. Nat. Commun. *6*, 10068.

Fang, J., Yang, J., Wu, X., Zhang, G., Li, T., Wang, X., Zhang, H., Wang, C.C., Liu, G.H., and Wang, L. (2018). Metformin alleviates human cellular aging by upregulating the endoplasmic reticulum glutathione peroxidase 7. Aging Cell. Published online April 16, 2018. https://doi.org/10.1111/acel.12765.

Flachsbart, F., Dose, J., Gentschew, L., Geismann, C., Caliebe, A., Knecht, C., Nygaard, M., Badarinarayan, N., ElSharawy, A., May, S., et al. (2018). Publisher Correction: Identification and characterization of two functional variants in the human longevity gene FOXO3. Nat. Commun. *9*, 320.

Fluteau, A., Ince, P.G., Minett, T., Matthews, F.E., Brayne, C., Garwood, C.J., Ratcliffe, L.E., Morgan, S., Heath, P.R., Shaw, P.J., et al.; MRC Cognitive Function Ageing Neuropathology Study Group (2015). The nuclear retention of transcription factor FOXO3a correlates with a DNA damage response and increased glutamine synthetase expression by astrocytes suggesting a neuroprotective role in the ageing brain. Neurosci. Lett. *609*, 11–17.

Geng, L., Liu, Z., Zhang, W., Li, W., Wu, Z., Wang, W., Ren, R., Su, Y., Wang, P., Sun, L., et al. (2018). Chemical screen identifies a geroprotective role of quercetin in premature aging. Protein Cell. Published online August 1, 2018. https://doi.org/10.1007/s13238-018-0567-y.

Ha, G., Roth, A., Lai, D., Bashashati, A., Ding, J., Goya, R., Giuliany, R., Rosner, J., Oloumi, A., Shumansky, K., et al. (2012). Integrative analysis of genome-wide loss of heterozygosity and monoallelic expression at nucleotide resolution reveals disrupted pathways in triple-negative breast cancer. Genome Res. *22*, 1995–2007.

Hahn, W.C., Dessain, S.K., Brooks, M.W., King, J.E., Elenbaas, B., Sabatini, D.M., DeCaprio, J.A., and Weinberg, R.A. (2002). Enumeration of the simian virus 40 early region elements necessary for human cell transformation. Mol. Cell. Biol. *22*, 2111–2123.

Harvey, A., Montezano, A.C., and Touyz, R.M. (2015). Vascular biology of ageing-Implications in hypertension. J. Mol. Cell. Cardiol. *83*, 112–121.

He, Y.H., Lu, X., Yang, L.Q., Xu, L.Y., and Kong, Q.P. (2014). Association of the insulin-like growth factor binding protein 3 (IGFBP-3) polymorphism with longevity in Chinese nonagenarians and centenarians. Aging (Albany N.Y.) *6*, 944–956.

Hentze, H., Graichen, R., and Colman, A. (2007). Cell therapy and the safety of embryonic stem cell-derived grafts. Trends Biotechnol. *25*, 24–32.

Ihry, R.J., Worringer, K.A., Salick, M.R., Frias, E., Ho, D., Theriault, K., Kommineni, S., Chen, J., Sondey, M., Ye, C., et al. (2018). p53 inhibits CRISPR-Cas9 engineering in human pluripotent stem cells. Nat. Med. *24*, 939–946.

Joyce, N., Annett, G., Wirthlin, L., Olson, S., Bauer, G., and Nolta, J.A. (2010). Mesenchymal stem cells for the treatment of neurodegenerative disease. Regen. Med. *5*, 933–946.

Keating, A. (2012). Mesenchymal stromal cells: new directions. Cell Stem Cell *10*, 709–716.

Kotlyar, M., Pastrello, C., Sheahan, N., and Jurisica, I. (2016). Integrated interactions database: tissue-specific view of the human and model organism interactomes. Nucleic Acids Res. *44* (D1), D536–D541.

Krueger, F., and Andrews, S.R. (2011). Bismark: a flexible aligner and methylation caller for Bisulfite-Seq applications. Bioinformatics *27*, 1571–1572.

Laina, A., Stellos, K., and Stamatelopoulos, K. (2018). Vascular ageing: Underlying mechanisms and clinical implications. Exp. Gerontol. *109*, 16–30.

Latonen, L., Järvinen, P.M., Suomela, S., Moore, H.M., Saarialho-Kere, U., and Laiho, M. (2010). Ultraviolet B radiation regulates cysteine-rich protein 1 in human keratinocytes. Photodermatol. Photoimmunol. Photomed. *26*, 70–77.

Laurent, S. (2012). Defining vascular aging and cardiovascular risk. J. Hypertens. *30* (*Suppl*), S3–S8.

Li, H., Handsaker, B., Wysoker, A., Fennell, T., Ruan, J., Homer, N., Marth, G., Abecasis, G., and Durbin, R.; 1000 Genome Project Data Processing Subgroup (2009). The Sequence Alignment/Map format and SAMtools. Bioinformatics *25*, 2078–2079.

Lian, Q., Zhang, Y., Zhang, J., Zhang, H.K., Wu, X., Zhang, Y., Lam, F.F., Kang, S., Xia, J.C., Lai, W.H., et al. (2010). Functional mesenchymal stem cells derived from human induced pluripotent stem cells attenuate limb ischemia in mice. Circulation *121*, 1113–1123.

Liu, G.H., Suzuki, K., Qu, J., Sancho-Martinez, I., Yi, F., Li, M., Kumar, S., Nivet, E., Kim, J., Soligalla, R.D., et al. (2011). Targeted gene correction of laminopathy-associated LMNA mutations in patient-specific iPSCs. Cell Stem Cell *8*, 688–694.

Liu, G.H., Qu, J., Suzuki, K., Nivet, E., Li, M., Montserrat, N., Yi, F., Xu, X., Ruiz, S., Zhang, W., et al. (2012). Progressive degeneration of human neural stem cells caused by pathogenic LRRK2. Nature *491*, 603–607.

Liu, G.H., Suzuki, K., Li, M., Qu, J., Montserrat, N., Tarantino, C., Gu, Y., Yi, F., Xu, X., Zhang, W., et al. (2014). Modelling Fanconi anemia pathogenesis and therapeutics using integration-free patient-derived iPSCs. Nat. Commun. *5*, 4330.

López-Otín, C., Blasco, M.A., Partridge, L., Serrano, M., and Kroemer, G. (2013). The hallmarks of aging. Cell *153*, 1194–1217.

Maguire, G. (2016). Therapeutics from Adult Stem Cells and the Hype Curve. ACS Med. Chem. Lett. *7*, 441–443.

Mahla, R.S. (2016). Stem Cells Applications in Regenerative Medicine and Disease Therapeutics. Int. J Cell Biol., 6940283–6940283.

Mali, P., Yang, L., Esvelt, K.M., Aach, J., Guell, M., DiCarlo, J.E., Norville, J.E., and Church, G.M. (2013). RNA-guided human genome engineering via Cas9. Science *339*, 823–826.

Martins, R., Lithgow, G.J., and Link, W. (2016). Long live FOXO: unraveling the role of FOXO proteins in aging and longevity. Aging Cell *15*, 196–207.

Medema, R.H., Kops, G.J.P.L., Bos, J.L., and Burgering, B.M.T. (2000). AFX-like Forkhead transcription factors mediate cell-cycle regulation by Ras and PKB through p27kip1. Nature *404*, 782–787.

Mikael, L.R., Paiva, A.M.G., Gomes, M.M., Sousa, A.L.L., Jardim, P.C.B.V., Vitorino, P.V.O., Euzébio, M.B., Sousa, W.M., and Barroso, W.K.S. (2017). Vascular Aging and Arterial Stiffness. Arq. Bras. Cardiol. *109*, 253–258.

Morris, B.J., Willcox, D.C., Donlon, T.A., and Willcox, B.J. (2015). FOXO3: A Major Gene for Human Longevity–A Mini-Review. Gerontology *61*, 515–525.

Murray, I.R., West, C.C., Hardy, W.R., James, A.W., Park, T.S., Nguyen, A., Tawonsawatruk, T., Lazzari, L., Soo, C., and Péault, B. (2014). Natural history of mesenchymal stem cells, from vessel walls to culture vessels. Cell. Mol. Life Sci. *71*, 1353–1374.

Ni, Y.G., Berenji, K., Wang, N., Oh, M., Sachan, N., Dey, A., Cheng, J., Lu, G., Morris, D.J., Castrillon, D.H., et al. (2006). Foxo transcription factors blunt cardiac hypertrophy by inhibiting calcineurin signaling. Circulation *114*, 1159–1168.

Niemistö, A., Dunmire, V., Yli-Harja, O., Zhang, W., and Shmulevich, I. (2005). Robust quantification of in vitro angiogenesis through image analysis. IEEE Trans. Med. Imaging *24*, 549–553.

Omae, M., Takada, N., Yamamoto, S., Nakajima, H., and Sato, T.N. (2013). Identification of inter-organ vascular network: vessels bridging between organs. PLoS ONE *8*, e65720.

Orlova, V.V., van den Hil, F.E., Petrus-Reurer, S., Drabsch, Y., Ten Dijke, P., and Mummery, C.L. (2014). Generation, expansion and functional analysis of endothelial cells and pericytes derived from human pluripotent stem cells. Nat. Protoc. *9*, 1514–1531.

Paik, J.H. (2006). FOXOs in the maintenance of vascular homoeostasis. Biochem. Soc. Trans. *34*, 731–734.

Paik, J.H., Kollipara, R., Chu, G., Ji, H., Xiao, Y., Ding, Z., Miao, L., Tothova, Z., Horner, J.W., Carrasco, D.R., et al. (2007). FoxOs are lineage-restricted redundant tumor suppressors and regulate endothelial cell homeostasis. Cell *128*, 309–323.

Pan, H., Guan, D., Liu, X., Li, J., Wang, L., Wu, J., Zhou, J., Zhang, W., Ren, R., Zhang, W., et al. (2016). SIRT6 safeguards human mesenchymal stem cells from oxidative stress by coactivating NRF2. Cell Res. *26*, 190–205.

Patsch, C., Challetmeylan, L., Thoma, E.C., Urich, E., Heckel, T., O'Sullivan, J.F., Grainger, S.J., Kapp, F.G., Lin, S., and Christensen, K. (2015). Generation of vascular endothelial and smooth muscle cells from human pluripotent stem cells. Nat. Cell Biol. *17*, 994–1003.

Pomiès, P., Louis, H.A., and Beckerle, M.C. (1997). CRP1, a LIM domain protein implicated in muscle differentiation, interacts with alpha-actinin. J. Cell Biol. *139*, 157–168.

Rahmati, S., Abovsky, M., Pastrello, C., and Jurisica, I. (2017). pathDIP: an annotated resource for known and predicted human gene-pathway associations and pathway enrichment analysis. Nucleic Acids Res. *45* (D1), D419–D426.

Regina, C., Panatta, E., Candi, E., Melino, G., Amelio, I., Balistreri, C.R., Annicchiarico-Petruzzelli, M., Di Daniele, N., and Ruvolo, G. (2016). Vascular ageing and endothelial cell senescence: Molecular mechanisms of physiology and diseases. Mech. Ageing Dev. *159*, 14–21.

Resnick, I.B., Barkats, C., Shapira, M.Y., Stepensky, P., Bloom, A.I., Shimoni, A., Mankuta, D., Varda-Bloom, N., Rheingold, L., Yeshurun, M., et al. (2013). Treatment of severe steroid resistant acute GVHD with mesenchymal stromal cells (MSC). Am. J. Blood Res. *3*, 225–238.

Santos, M.A., Faryabi, R.B., Ergen, A.V., Day, A.M., Malhowski, A., Canela, A., Onozawa, M., Lee, J.E., Callen, E., Gutierrez-Martinez, P., et al. (2014). DNA-damage-induced differentiation of leukaemic cells as an anti-cancer barrier. Nature *514*, 107–111.

Scaffidi, P., and Misteli, T. (2011). In vitro generation of human cells with cancer stem cell properties. Nat. Cell Biol. *13*, 1051–1061.

Schmeichel, K.L., and Beckerle, M.C. (1998). LIM domains of cysteine-rich protein 1 (CRP1) are essential for its zyxin-binding function. Biochem. J. *331*, 885–892.

Schwank, G., Koo, B.K., Sasselli, V., Dekkers, J.F., Heo, I., Demircan, T., Sasaki, N., Boymans, S., Cuppen, E., van der Ent, C.K., et al. (2013). Functional repair of CFTR by CRISPR/Cas9 in intestinal stem cell organoids of cystic fibrosis patients. Cell Stem Cell *13*, 653–658.

Smallwood, S.A., Lee, H.J., Angermueller, C., Krueger, F., Saadeh, H., Peat, J., Andrews, S.R., Stegle, O., Reik, W., and Kelsey, G. (2014). Single-cell genome-wide bisulfite sequencing for assessing epigenetic heterogeneity. Nat. Methods *11*, 817–820.

Squillaro, T., Peluso, G., and Galderisi, U. (2016). Clinical Trials With Mesenchymal Stem Cells: An Update. Cell Transplant. *25*, 829–848.

Suzuki, K., Yu, C., Qu, J., Li, M., Yao, X., Yuan, T., Goebl, A., Tang, S., Ren, R., Aizawa, E., et al. (2014). Targeted gene correction minimally impacts whole-genome mutational load in human-disease-specific induced pluripotent stem cell clones. Cell Stem Cell *15*, 31–36.

Suzuki, K., Tsunekawa, Y., Hernandez-Benitez, R., Wu, J., Zhu, J., Kim, E.J., Hatanaka, F., Yamamoto, M., Araoka, T., Li, Z., et al. (2016). In vivo genome editing via CRISPR/Cas9 mediated homology-independent targeted integration. Nature *540*, 144–149.

Reya, T., Duncan, A.W., Ailles, L., Domen, J., Scherer, D.C., Willert, K., Hintz, L., Nusse, R., and Weissman, I.L. (2003). A role for Wnt signalling in self-renewal of haematopoietic stem cells. Nature *423*, 409–414.

Tompkins, B., Balkan, W., and Hare, J.M. (2015). Perspectives on the Evolution of Stem Cell Therapy for Heart Failure. EBioMedicine *2*, 1838–1839.

Trapnell, C., Pachter, L., and Salzberg, S.L. (2009). TopHat: discovering splice junctions with RNA-Seq. Bioinformatics *25*, 1105–1111.

Trapnell, C., Williams, B.A., Pertea, G., Mortazavi, A., Kwan, G., van Baren, M.J., Salzberg, S.L., Wold, B.J., and Pachter, L. (2010). Transcript assembly and quantification by RNA-Seq reveals unannotated transcripts and isoform switching during cell differentiation. Nat. Biotechnol. *28*, 511–515.

Trapnell, C., Roberts, A., Goff, L., Pertea, G., Kim, D., Kelley, D.R., Pimentel, H., Salzberg, S.L., Rinn, J.L., and Pachter, L. (2012). Differential gene and transcript expression analysis of RNA-seq experiments with TopHat and Cufflinks. Nat. Protoc *7*, 562–578.

Trounson, A., and McDonald, C. (2015). Stem Cell Therapies in Clinical Trials: Progress and Challenges. Cell Stem Cell *17*, 11–22.

Tsai, W.B., Chung, Y.M., Takahashi, Y., Xu, Z., and Hu, M.C. (2008). Functional interaction between FOXO3a and ATM regulates DNA damage response. Nat. Cell Biol. *10*, 460–467.

van der Horst, A., and Burgering, B.M. (2007). Stressing the role of FoxO proteins in lifespan and disease. Nat. Rev. Mol. Cell Biol. *8*, 440–450.

Wang, Y., Han, Z.B., Song, Y.P., and Han, Z.C. (2012). Safety of mesenchymal stem cells for clinical application. Stem Cells Int. *2012*, 652034.

Wang, L., Yi, F., Fu, L., Yang, J., Wang, S., Wang, Z., Suzuki, K., Sun, L., Xu, X., Yu, Y., et al. (2017). CRISPR/Cas9-mediated targeted gene correction in amyotrophic lateral sclerosis patient iPSCs. Protein Cell *8*, 365–378.

Wang, P., Liu, Z., Zhang, X., Li, J., Sun, L., Ju, Z., Li, J., Chan, P., Liu, G.H., Zhang, W., et al. (2018a). CRISPR/Cas9-mediated Gene Knockout Reveals a Guardian Role of NF-kB/RelA in Maintaining the Homeostasis of Human Vascular Cells. Protein Cell *9*, 945–965.

Wang, S., Hu, B., Ding, Z., Dang, Y., Wu, J., Li, D., Liu, X., Xiao, B., Zhang, W., Ren, R., et al. (2018b). ATF6 safeguards organelle homeostasis and cellular aging in human mesenchymal stem cells. Cell Discov. *4*, 2.

Willcox, B.J., Donlon, T.A., He, Q., Chen, R., Grove, J.S., Yano, K., Masaki, K.H., Willcox, D.C., Rodriguez, B., and Curb, J.D. (2008). FOXO3A genotype is strongly associated with human longevity. Proc. Natl. Acad. Sci. USA *105*, 13987–13992.

Wiznerowicz, M., and Trono, D. (2003). Conditional suppression of cellular genes: lentivirus vector-mediated drug-inducible RNA interference. J. Virol. *77*, 8957–8961.

Wu, J., Lee, S.W., Zhang, X., Han, F., Kwan, S.Y., Yuan, X., Yang, W.L., Jeong, Y.S., Rezaeian, A.H., Gao, Y., et al. (2013). Foxo3a transcription factor is a negative regulator of Skp2 and Skp2 SCF complex. Oncogene *32*, 78–85.

Wu, Z., Zhang, W., Song, M., Wang, W., Wei, G., Li, W., Lei, J., Huang, Y., Sang, Y., Chan, P., et al. (2018). Differential stem cell aging kinetics in Hutchinson-Gilford progeria syndrome and Werner syndrome. Protein Cell *9*, 333–350.

Yang, J., Li, J., Suzuki, K., Liu, X., Wu, J., Zhang, W., Ren, R., Zhang, W., Chan, P., Izpisua Belmonte, J.C., et al. (2017). Genetic enhancement in cultured human adult stem cells conferred by a single nucleotide recoding. Cell Res. *27*, 1178–1181.

Zengin, E., Chalajour, F., Gehling, U.M., Ito, W.D., Treede, H., Lauke, H., Weil, J., Reichenspurner, H., Kilic, N., and Ergün, S. (2006). Vascular wall resident progenitor cells: a source for postnatal vasculogenesis. Development *133*, 1543–1551.

Zhang, W., Li, J., Suzuki, K., Qu, J., Wang, P., Zhou, J., Liu, X., Ren, R., Xu, X., Ocampo, A., et al. (2015). Aging stem cells. A Werner syndrome stem cell model unveils heterochromatin alterations as a driver of human aging. Science *348*, 1160–1163.

Zhang, H., Zhao, Z., Pang, X., Yang, J., Yu, H., Zhang, Y., Zhou, H., and Zhao, J. (2017). MiR-34a/sirtuin-1/foxo3a is involved in genistein protecting against ox-LDL-induced oxidative damage in HUVECs. Toxicol. Lett. *277*, 115–122.

Zhang, W., Song, M., Qu, J., and Liu, G.-H. (2018). Epigenetic Modifications in Cardiovascular Aging and Diseases. Circ. Res. *123*, 773–786.

Zhao, M., Sun, J., and Zhao, Z. (2013). TSGene: a web resource for tumor suppressor genes. Nucleic Acids Res. *41*, D970–D976.

Zhu, P., Guo, H., Ren, Y., Hou, Y., Dong, J., Li, R., Lian, Y., Fan, X., Hu, B., Gao, Y., et al. (2018). Single-cell DNA methylome sequencing of human preimplantation embryos. Nat. Genet. *50*, 12–19.

STAR★METHODS

KEY RESOURCES TABLE

REAGENT or RESOURCE	SOURCE	IDENTIFIER
Antibodies		
Rabbit monoclonal anti-FOXO3	Cell Signaling Technology	Cat#2497S; RRID: AB_836876
Rabbit polyclonal anti-RanBP2 (Nup358)	Abcam	Cat# ab64276, RRID:AB_1142517
Rabbit polyclonal anti-NANOG	Abcam	Cat# ab21624, RRID:AB_446437
Mouse monoclonal anti-OCT3/4	Santa Cruz	Cat# sc-5279, RRID:AB_628051
Goat polyclonal anti-SOX2	Santa Cruz	Cat# sc-17320, RRID:AB_2286684
Rabbit polyclonal anti-β-Tubulin III (Tuj1)	Sigma-Aldrich	Cat# T2200, RRID:AB_262133
Rabbit monoclonal anti-FOXA2	Cell Signaling Technology	Cat# 8186S, RRID:AB_10892612
Mouse monoclonal anti-SMA	Sigma-Aldrich	Cat# A5228, RRID:AB_262054
Mouse monoclonal anti-CD31	BD Biosciences	Cat# 555445, RRID:AB_395838
Rabbit polyclonal anti-vWF	Dako	Cat# A0082, RRID:AB_2315602
Rabbit polyclonal anti-VE-Cadherin	Cell Signaling Technology	Cat# 2158S, RRID:AB_10692903
Rabbit polyclonal anti-SM22	Abcam	Cat# ab14106, RRID:AB_443021
Mouse monoclonal anti-Calponin	Dako	Cat# M3556, RRID:AB_2082148
Rabbit monoclonal anti-Ki67	Vector Laboratories	Cat# VP-RM04, RRID:AB_2336545
Alexa Fluor 594 Phalloidin (F-actin)	Thermo Fisher Scientific	Cat# A12381, RRID:AB_2315633
Mouse monoclonal anti-LAP2	BD Biosciences	Cat# 611000, RRID:AB_398313
Rat monoclonal anti-CD73	BD Biosciences	Cat# 550741, RRID:AB_393860
Mouse monoclonal anti-CD90	BD Biosciences	Cat# 555595, RRID:AB_395969
Mouse monoclonal anti-CD105	Thermo Fisher Scientific	Cat# 17-1057-42, RRID:AB_1582211
Mouse monoclonal anti-CD31	BD Biosciences	Cat# 555445, RRID:AB_395838
Mouse monoclonal anti-CD34	BD Biosciences	Cat# 555822, RRID:AB_396151
Mouse monoclonal anti-CD43	BD Biosciences	Cat# 560198, RRID:AB_1645460
Mouse monoclonal anti-CD45	BD Biosciences	Cat# 555482, RRID:AB_395874
Mouse monoclonal anti-CD144	BD Biosciences	Cat# 560410, RRID:AB_1645502
Mouse monoclonal anti-CD140b	BD Biosciences	Cat# 558821, RRID:AB_397132
Mouse monoclonal anti-SIRT1	Santa Cruz	Cat# sc-74504, RRID:AB_2188348
Rabbit polyclonal anti-H3K9ac	Abcam	Cat# ab4441, RRID:AB_2118292
Rabbit polyclonal anti-H3K4me3	Abcam	Cat# ab8580, RRID:AB_306649
Rabbit polyclonal anti-H3K9me3	Abcam	Cat# ab8898, RRID:AB_306848
Mouse monoclonal anti-LAP2	BD Biosciences	Cat# 611000, RRID:AB_398313
Rabbit polyclonal anti-Lamin B1	Abcam	Cat# ab16048, RRID:AB_443298
Mouse monoclonal anti-Histone H2A.X, phospho (Ser139)	Millipore	Cat# 05-636, RRID:AB_309864
Rabbit polyclonal anti-53BP1	Bethyl	Cat# A300-273A, RRID:AB_185521
Rabbit polyclonal anti-CSRP1	Abcam	Cat# ab70010, RRID:AB_1268316
Rabbit polyclonal anti-WRN	Abcam	Cat# ab200, RRID:AB_302751
Mouse monoclonal anti-FLAG	Sigma-Aldrich	Cat# F1804, RRID:AB_262044
Mouse monoclonal anti-β-Tubulin	Santa Cruz	Cat# sc-5274, RRID:AB_2288090
Mouse monoclonal anti-β-Actin	Santa Cruz	Cat# sc-69879, RRID:AB_1119529
Rabbit polyclonal anti-GAPDH	Santa Cruz	Cat# sc-25778, RRID:AB_10167668
Biological Samples		
Human dental pulp tissue	306 hospital of PLA in Beijing	N/A
Chemicals, Peptides, and Recombinant Proteins		
Matrigel	Matrigel Matrix	Cat# 354230
STEMCELL mTeSR1	STEMCELL Technology	Cat# 05850

(*Continued on next page*)

Continued

REAGENT or RESOURCE	SOURCE	IDENTIFIER
Collagen IV	Biocoat	Cat# 354233
EGM2	LONZA	Cat# CC-3162
SB431542	Selleck Chemicals	S1067; CAS: 301836-41-9
VEGF	Stem Immune	Cat# HVG-VF5-1000
bFGF	Joint Protein Central	Cat# BBI-EXP-002
PDGF-AB	Pepro Tech	Cat# 100-00AB
IWP2	Selleck Chemicals	S7085; CAS: 686770-61-6
BMP4	R&D systems	Cat# 314-BP
CHIR99021	Selleck Chemicals	S1263; CAS: 252917-06-9
IL6	Pepro Tech	Cat# 200-06;
HEPES	Sigma-Aldrich	Cat# H3375; CAS: 7365-45-9
NP-40	Dingguo	Cat# DH218
DTT	Amresco	Cat# Amr-0281; CAS: 3483-12-3
Protease inhibitor cocktail	Roche	Cat# 4693159001
EDTA	Sigma-Aldrich	Cat# EDS; CAS: 60-00-4
Triton X-100	Sigma-Aldrich	Cat# T9284; CAS: 9002-93-1
G418	Thermo Fisher Scientific	Cat# 11811023; CAS: 108321-42-2
Zeocin	InvivoGen	Cat# ant-zn-05; CAS: 11006-33-0
Puromycin	InvivoGen	Cat# ant-pr-1; CAS: 58-58-2
Lipofectamine 3000 Reagent	Thermo Fisher Scientific	Cat# L3000015
Critical Commercial Assays		
GeneTailor Site-Directed Mutagenesis System	Invitrogen	Cat# 12397-014
CpGenome Fast DNA Modification kit	Millipore	Cat# S7824
Dual-Luciferase assay kit	Vigorous Biotechnology	Cat# T002
Annexin V-EGFP Apoptosis Detection Kit	Vigorous Biotechnology	Cat# A002
Fast MultiSite Mutagenesis System	TRANSGEN BIOTECH	Cat# FM201-01
GoScript Reverse Transcription System	Promega	Cat# A5001
RNeasy Mini Kit	QIAGEN	Cat# 74106
Next Poly (A) mRNA Magnetic Isolation Module	New England Biolabs	Cat# E7490L
Next ultra RNA library prep kit for Illumina	New England Biolabs	Cat# E7530L
Agencourt AMPure XP beads	Beckman Coulter	Cat# A63882
DNeasy Blood & Tissue Kit	QIAGEN	Cat# 69506
Qubit dsDNA HS Assay Kit	Invitrogen	Cat# Q32854
NEBNext ultra DNA library prep kit for Illumina	New England Biolabs	Cat# E7370L
EZ-96 DNA Methylation-DirectMagPrep	Zymo	Cat# D5044
dNTP Mixture	TAKARA	Cat# 4019
Klenow (3′ → 5′ exo-)	Enzymatic	Cat# P7010-HC-L
Exonuclease I	New England Biolabs	Cat# M0293L
Dynabeads M-280 Streptavidin	Invitrogen	Cat# 11206D
KAPA HiFi HotStart ReadyMix	Kapa Biosystems	Cat# KK2602
Deposited Data		
Raw sequencing data (RNA, CNV and DNA methylation)	This paper	GEO: GSE116277
Experimental Models: Cell Lines		
HEK293T	ATCC	Cat# CRL-1573
Wildtype hESCs (Line H9)	WiCell Research	Cat# WA09
Human vascular endothelial cells derived from hESCs	This paper	N/A

(*Continued on next page*)

Continued

REAGENT or RESOURCE	SOURCE	IDENTIFIER
Human vascular smooth muscle cells derived from hESCs	This paper	N/A
Human mesenchymal stem cells derived from hESCs	This paper	N/A
Transformed hMSCs	This paper	N/A
Primary hMSC from human dental pulp tissue	This paper	N/A
Experimental Models: Organisms/Strains		
Mouse: CAnN.Cg-Foxn1^{nu}/Crl	Charles River	N/A
Mouse: NOD.CB17-Prkdc^{scid}/NcrCrl	Charles River	N/A
Mouse: NOD-Prkdc^{scid} IL2rg^{tm1}/Bcgen	Biocytogen	N/A
Recombinant DNA		
Helper-dependent adenoviral vector (HDAdV) for *FOXO3*$^{2SA/2SA}$	This paper	N/A
pCR2.1-TOPO	Thermo Fisher Scientific	Cat# K455001
pAMHDAdGT8-4	A gift from Kohnosuke Mitani	Addgene plasmid #26421
gRNA_Cloning Vector	(Brunet et al., 1999; Counter et al., 1998; Mali et al., 2013; Reya et al., 2003; Wiznerowicz and Trono, 2003)	Addgene plasmid #41824
pCAG-1BPNLS-Cas9-1BPNLS-2AGFP	(Suzuki et al., 2016)	Addgene plasmid #87109
pCAGmCherry-gRNA	(Suzuki et al., 2016)	Addgene plasmid #87110
pLVTHM	(Wiznerowicz and Trono, 2003)	Addgene plasmid #12247
psPAX2	A gift from Didier Trono	Addgene plasmid #12260
pMD2.G	A gift from Didier Trono	Addgene plasmid #12259
pBABE-neo-hTERT	(Counter et al., 1998)	Addgene plasmid #1774
pBABE-zeo largeTgenomic	(Hahn et al., 2002)	Addgene plasmid #1778
pBabe-puro Ras V12	A gift from Bob Weinberg	Addgene plasmid #1768
gag/pol	(Reya et al., 2003)	Addgene plasmid #14887
VSV.G	(Reya et al., 2003)	Addgene plasmid #14888
FHRE-Luc	(Brunet et al., 1999)	Addgene plasmid #1789
pGL3-Basic Vector	Promega	Cat# E1751
Software and Algorithms		
Image Lab	Bio-rad	http://www.bio-rad.com/zh-cn/product/image-lab-software?ID=KRE6P5E8Z
FlowJo	Flowjo, LLC	https://www.flowjo.com/
ImageJ	NIH	https://imagej.nih.gov/ij/
Leica LAS AF Lite version 2.6.0	Leica	https://leica-las-af-lite.updatestar.com/
GraphPadPrism 6.0	GraphPad Software Inc.	https://www.graphpad.com/
AngioQuant	(Niemistö et al., 2005)	http://www.cs.tut.fi/sgn/csb/angioquant/

CONTACT FOR REAGENT AND RESOURCE SHARING

Further information and requests for resources and reagents should be directed to and will be fulfilled by the Lead Contact, Guang-Hui Liu (ghliu@ibp.ac.cn).

EXPERIMENTAL MODEL AND SUBJECT DETAILS

Mouse Models

All animal experiments conducted in this study were approved by the Chinese Academy of Science Institutional Animal Care and Use Committee. Immunodeficient male NOD-SCID (4-8 weeks old) and BALB/c nude (8-10 weeks old) mice have been purchased from Charles River Laboratories and bred, raised and housed in the Laboratory of Immunodeficiency animals of Institute of Biophysics, Chinese Academy of Sciences with 12-hour light/dark cycle and provided with food and water *ad libitum* according to Charles River

Laboratories recommendation (strain codes: 406 and 401, respectively). All mice were healthy with no obvious behavioral phenotypes.

Cell Culture

Wild-type hESCs (Line H9, female) and derived *FOXO3*$^{2SA/2SA}$ hESCs were cultured on Mitomycin C-inactivated mouse embryonic fibroblasts (MEF) with cDF12 medium or Matrigel-coated plates with mTeSR1 medium, as previously described (Duan et al., 2015; Pan et al., 2016). hVECs were maintained on collagen-coated plates in EGM2 medium supplemented with 10 nM SB431542, 50 ng/mL VEGF and 20 ng/mL bFGF. hVSMCs were cultured in VSMC medium with 10 ng/ml PDGF-AB, as previously described (Wang et al., 2018a). Human ESC derived-MSCs and human dental pulp-derived primary MSCs were cultured in α-MEM medium supplemented with 10% fetal bovine serum, 0.1 mM non-essential amino acids, 1% penicillin/streptomycin, and 1 ng/ml bFGF. hTMSCs were maintained in hMSC medium without bFGF. No mycoplasma contamination was observed during cell culture.

METHOD DETAILS

Generation of FOXO3-enhanced hESCs

Helper-dependent adenoviral vector (HDAdV) for *FOXO3*$^{2SA/2SA}$ (Ser253Ala and Ser315Ala) knock-in was generated as previously described, with some modifications (Liu et al., 2014; Liu et al., 2011). In brief, part of intron 2 and exon 3 of the *FOXO3* gene was PCR-amplified from RP11-653O20 BAC DNA (BACPAC Resources) and subcloned into the pCR2.1-TOPO vector. The Ser253Ala and Ser315Ala mutations at exon 3 were introduced using the GeneTailor Site-Directed Mutagenesis System (Invitrogen). An *FRT*-PGK-EM7-neo-bpA-*FRT* marker fragment was subcloned into intron 2 in the 2SA mutated plasmid, and the generated DNA fragment was recombined into RP11-653O20 BAC DNA using BAC recombineering (Datsenko and Wanner, 2000). A total of 20.9 kb of homology arms for *FOXO3* gene, including the Ser253Ala and Ser315Ala mutations and marker cassette, was subcloned into the HDAdV backbone plasmid pAMHDAdGT8-4 (Addgene #26421). The generated plasmids were packaged into HDAdVs following a previous report (Yang et al., 2017). To generate heterozygous *FOXO3*$^{2SA/2SA}$ mutation knock-in hESCs, hESCs were infected with *FOXO3*$^{2SA/2SA}$ HDAdV at MOI of 0.6-6, as described previously (Yang et al., 2017). To generate homozygous *FOXO3*$^{2SA/2SA}$ hESCs, we repeated a second round of mutation knock-in using the generated heterozygous *FOXO3*$^{2SA/2SA}$ clones.

Generation of WRN-Deficient FOXO3 S253A and S315A Knock-in hESCs

The WRN protein in *FOXO3*$^{2SA/2SA}$ hESCs was ablated using CRISPR/Cas9 following previously described protocols with minor modifications (Wang et al., 2018a; Wang et al., 2018b). Briefly, the gRNA (TACATAAACAGGTGGATAC) targeting exon 14 of WRN gene was cloned into a gRNA vector (Addgene #41824)(Mali et al., 2013). Briefly, 5 × 10^6 hESCs were dissociated using TrypLE, then electorporated with pCAG-1BPNLS-Cas9-1BPNLS-2AGFP (Addgene #87109) and pCAGmCherry-gRNA (Addgene #87110) vectors (Suzuki et al., 2016). After two days mCherry$^+$/GFP$^+$ cells were isolated by FACS (BD FACS Aria II). After about two weeks in culture, a single clone was picked into a 96-well culture plate and expanded for identification. Primers are shown in Table S5.

Directed Differentiation of hESCs into hVECs

Differentiation of hESCs into hVECs was performed as previously described with minor modifications (Patsch et al., 2015). Briefly, hESCs were cultured in mTeSR1-media for one day and then in M1 medium, containing IWP2 (3 μM), BMP4 (25 ng/ml), CHIR99021 (3 μM) and bFGF (4 ng/ml), for three days. The following day, M1 medium was removed and replaced with M2 medium with the addition of VEGF (50 ng/ml), bFGF (20 ng/ml) and IL6 (10 ng/ml) to promote endothelial cell emergence for another three days. The differentiated adherent cells were harvested using TrypLE (GIBCO), and then counted upon anti-human CD201 and CD34 staining. Flow cytometry detection of cell surface antigens and cell sorting were performed on BD FACS Aria II.

Directed Differentiation of hESCs into hVSMCs

Differentiation of hESCs into hVSMCs was performed as previously described with minor modifications (Wang et al., 2018a). First, after 4-5 days in culture in mTeSR1 medium on matrigel coated plates, the hESCs were dissociated into single cells using TrypLE and seeded onto matrigel-coated plates at a concentration of 3 × 10^4 cells/cm^2. The following day, cells were cultured in M1 medium for three days and then in M2 medium for two days. At day 5, cells were harvested with TrypLE, purified with CD140b by FACS Aria II and cultured on collagen IV-coated plates with VSMC culture medium.

Directed Differentiation of hESCs into hMSCs

Differentiation of hESCs into hMSCs was performed as previously described (Fang et al., 2018; Yang et al., 2017). In brief, embryoid bodies were cultured in hMSC differentiation medium (αMEM supplemented with 10% FBS, 10 ng/ml bFGF, 5 ng/ml TGFβ (Human-Zyme) and 1% penicillin/streptomycin) for 10 days until fibroblast-like cells appeared. The hMSCs were purified with hMSC-specific markers CD73, CD90, and CD105 by FACS Aria II. Negative hMSC markers CD34, CD43, and CD45 were also analyzed by FACS. Anti-IgG-FITC, anti-IgG-PE, and anti-IgG-APC antibodies were used as isotype controls. To evaluate the tri-lineage differentiation of hMSCs, cells were differentiated toward bone, cartilage, and adipocytes and assessed by histochemical staining with von Kossa (osteogenesis), Toluidine blue O (chondrogenesis), and Oil red O (adiopogenesis), respectively.

Isolation and Culture of Human Dental Pulp-Derived Primary MSCs

Primary MSCs were isolated from different individuals with the approval from the Ehics Committee of the 306 Hospital of PLA in Beijing. Briefly, the pulp tissues were cut into small pieces and digested with TrypLE^{TM} Express Enzyme plus Dispase IV at 37°C for 30 mins. The pellet was then cultured in MSC culture medium to grow primary MSCs. The sample information was described in Table S1.

Bisulfite Sequencing of the OCT4 Promoter

Bisulfite sequencing of the *OCT4* promoter was conducted as previously described (Duan et al., 2015). Briefly, bisulfite conversion of genomic DNA was carried out using the CpGenome Fast DNA Modification Kit following the manufacturer's protocol. The genomic fragment of the *OCT4* promoter was amplified using LA Taq Hot Start Version. PCR products were purified by gel extraction using QIAquick columns and cloned into the T-Vector pMD20. Six clones from each sample were picked and sequenced with the universal primer M13F.

Nuclear and Cytoplasmic Protein Extraction

About 1 × 10^6 living cells were lysed using buffer A (containing 10 mM HEPES-KOH pH 7.9, 10 mM KCl, 1.5 mM $MgCl_2$, 0.4% NP-40, 1 mM DTT) with 1x protease inhibitor cocktail. After centrifugation, the cytoplasmic fractions were collected. The remaining pellets were further lysed in buffer B (20 mM HEPES-KOH pH 7.9, 420 mM NaCl, 0.2 mM EDTA, 0.1 mM EGTA, 25% glycerin, 1 mM DTT) with 1 × protease inhibitor cocktail for the extraction of the nuclear fractions.

Protein, DNA and RNA Analysis

For western blot, cells were harvested and lysed in cold RIPA buffer. Protein quantification was performed using a BCA kit. Western blotting was performed as previously described (Zhang et al., 2015). For quantitative real-time PCR (RT-PCR), total RNA was extracted with TRIzol reagent and reverse transcribed to cDNA using GoScript Reverse Transcription System. RT-PCR was performed using THUNDERBIRD SYBR qPCR mix on a CFX384 Real-Time PCR system. Genomic DNA was extracted using a DNA extraction kit. PCR was performed with PrimeSTAR polymerase. To measure telomere length, qPCR was performed with genomic DNA as the template. Primer sequences for PCR are listed in Table S5.

Immunofluorescence

Cells were washed twice by PBS and fixed in 4% paraformaldehyde for 30 min. Cells were permeabilized in 0.4% Triton X-100 for 30 min and blocked in 10% donkey serum for 1 hr at room temperature. Cells were blocked and incubated with primary antibodies at 4°C overnight, and then with secondary antibodies as appropriate at room temperature for 1 hr. Nuclei were labeled using Hoechst 33342. A Leica SP5 confocal was used for immunofluorescence microscopy.

Flow Cytometry Analysis

For cell surface marker CD31, CD34, CD43, CD45, CD144 and CD140b analyses, 5 × 10^5 cells were incubated with antibodies for 30 min. For cellular apoptosis analysis, live cells were freshly harvested and stained with Annexin V-EGFP and PI. Notably, for assays of H_2O_2-induced hVSMC apoptosis, the medium for hVSMC culture was 2-Mecaptoethanol free in order to rule out any potential interference from the antioxidive effect of 2-Mecaptoethanol. For cellular ROS, live cells were collected and stained with 1 μM H2DCFDA for 30 min. Cell cycle was analyzed using Click-iT® EdU Alexa Fluor® 647 Flow Cytometry Assay Kit according to the manufacturer's recommendation. All experiments were performed on BD FACS Aria II.

SA-β-Gal Staining

SA-β-Gal staining was performed as previously described (Pan et al., 2016). In brief, cells were fixed in fixation buffer (2% formaldehyde and 0.2% glutaraldehyde) for 4 min at room temperature. After fixation, cells were stained with staining solution at 37°C overnight. The percentage of SA-β-Gal positive cells were quantified by ImageJ.

Clonal Expansion Assay

Clonal expansion assay was conducted as previously described (Geng et al., 2018). 2,000 hMSCs were seeded in each well of a gelatin-coated 12-well plate and cultured for 10 days. 2,000 hECs were seeded in each well of a collagen-coated 12-well plate and cultured for 12 days. Cells were fixed and stained with crystal violet and the relative cell number was counted by ImageJ.

Cell Migration Assay

The cell migration ability of hVECs was assessed by wound healing assay and trans-well assay. For the wound healing assay, hVECs were cultured in collagen-coated 12-well plates. Then, a linear scratch (''wound'') was generated using a 1 mL pipette tip in plates with cells at less than 100% confluency. Complete hVEC medium was added and cells were cultured for 20 hr at 37°C. Cells that migrated into the scratch were counted. For the transwell assay, the top chamber of the transwells (24-well insert; pore size, 8 μm; Corning Costar) was seeded with 2 × 10^4 cells in 500 μL IMDM medium. Another 500 μL of complete hVECs medium was added into the bottom chambers. After 24 hr, cells that migrated through the transwell were stained with crystal violet and counted by ImageJ.

In Vitro Matrigel Tube Formation

The hVECs were resuspended in complete hVEC medium and plated in 24-well plates coated with Matrigel at a density of 6×10^4 cells per well with three repeats. After 8 hr of incubation, photographs were taken under an optical microscope and analyzed by AngioQuant software (Niemistö et al., 2005).

Lentivirus and Retrovirus Production

For generating lentiviral vectors encoding shRNA targeting CSRP1, shRNA oligos were cloned into the pLVTHM vector (Addgene #12247) (Wiznerowicz and Trono, 2003). For packaging lentiviruses, HEK293T cells were co-transfected with lentiviral expression vectors or shRNA vectors, as well as psPAX2 (Addgene #12260) and pMD2.G (Addgene #12259). The pBABE-neo-hTERT, pBABEzeo-largeTgenomic and pBABE-puro-RasV12 retroviral vectors were purchased from Addgene (#1774, #1778, #1768). For packaging retrovirus, HEK293T cells were co-transfected with retroviral vectors, as well as gag/pol (Addgene #14887) and VSV.G (Addgene #14888) (Reya et al., 2003). Viral particles were collected by ultracentrifugation at 19,400 *g* for 2.5 hr.

Oncogenic Transformation

The *in vitro* oncogenic transformation was conducted based on previous reports (Scaffidi and Misteli, 2011). hMSCs were transduced sequentially with pBABE-neo-hTERT, pBABE-zeo-largeTgenomic and pBABE-puro-RasV12 retroviruses (Counter et al., 1998; Hahn et al., 2002). At the same time, cells were selected using G418 (100 μg/mL, 7 days), zeocin (100 μg/mL, 7 days) and puromycin (1 μg/mL, 3 days), respectively. The selected cells were transfected with the pLVTHM-shRNA-P53 vector for reducing P53 expression. The generated hTMSCs were regarded as passage 1 (P1) and cultured in hTMSC medium. Primers are shown in Table S5.

Anchorage-independent Growth Assay

To evaluate tumor formation ability *in vitro*, a soft agarose assay was conducted. First, 1×10^5 TMSCs suspended in 2 × TMSC medium mixed with an equal volume of 0.7% agarose were seeded onto the 0.6% agarose layers in 6-well plates. After four weeks, colonies were stained with 0.001% crystal violet for the measurement of relative colony sizes by ImageJ.

Animal Experiments

Teratoma-forming Assay

For the teratoma assay, 3×10^6 hESCs on Matrigel were injected into male NOD-SCID mice (6-8 weeks). After about two months, teratomas were collected and analyzed by immunostaining.

Hindlimb Ischemia Induction

The hindlimb ischemia was induced in male BALB/c nude mice (8-10 weeks) as previously described (Yang et al., 2017). Briefly, proximal and distal femoral artery were ligated using 7-0 nonabsorbable suture; then 3×10^6 cells or PBS (as negative control) were immediately injected into the ischemic hindlimb muscles of the mice. Primary hMSCs used for injection were isolated from the pulp tissue of a 28-year-old man. Blood perfusion was monitored every four days by the laser Doppler bloodperfusion (Moor instruments). 16 days after the ligation, hindlimb muscles were harvested for section staining. The degree of necrosis was classified into four grades: clinical score 0 (CS0, normal), clinical score 1 (CS1, toe gangrene), clinical score 2 (CS2, foot gangrene) and clinical score 3 (CS3, leg gangrene) (Cho et al., 2007). Hindlimb were fixed in 4% paraformaldehyde and embedded in O.C.T for section staining.

hMSC Tumor Susceptibility Test

For the hMSC tumor susceptibility test, 3×10^6 hMSCs (P5) suspended in 100 μL Matrigel/PBS (1:4) were injected into the 4- to 6-week-old male NOD-SCID mice (n = 7). Animals were checked every month to monitor the long-term *in vivo* consequences.

hTMSC Tumor-forming Assay

For the hTMSC tumor-forming assay, 3×10^6 hTMSCs suspended in 100 μL Matrigel/PBS (1:4) were injected into the 4- to 6-week-old male NOD-SCID mice (n = 6). About three months after transplantation, animals were sacrificed to evaluate the tumor-forming ability and legs with tumors were fixed in 4% paraformaldehyde and embedded in O.C.T for section staining.

Luciferase Reporter Assay

The FHRE-Luc vector (Addgene #1789) was used to evaluate FOXO3 transcriptional activity (Brunet et al., 1999). Partial *CSRP1* promoter was amplified by PCR and cloned into the pGL3-Basic vector. The mutant version of the pGL3-CSRP1 vector was constructed with Fast Mutagenesis System kit. The pGL3 vectors together with a Renilla plasmid were co-transfected into hMSCs with Lipofectamine 3000. After two days, cells were lysed for the measurement using the Dual-Luciferase assay kit.

ChIP-qPCR

ChIP-qPCR was performed according to a previous protocol with minor modifications (Wang et al., 2018b). In brief, cells were cross-linked using formaldehyde and lysed. Subsequently, a Bioruptor Plus sonication device (Diagenode) was used to shear the chromatin into fragments. After centrifugation, the supernatants were incubated overnight with Protein A dynabeads associated with 2.4 μg antibodies or control IgG. After elution at 68°C for 2 hr, DNA was purified by phenolchloroform-isoamylalcohol and chloroform-isoamylalcohol extractions. The enriched DNA was subjected to qPCR to evaluate target protein occupation at the *CSPR1* promoter region. The potential FOXO3 binding site at *CSRP1* promoter was predicted by using a bioinformatics website: (http://jaspar.genereg.net/). The primer sequences used for ChIP-qPCR are listed in Table S5.

RNA-seq Library Construction and Sequencing

Total RNA was extracted from 1 × 10^6 cells using RNeasy Mini Kit according to the manufacturer's instructions. The quality and quantity of total RNA was assessed by Fragment Analyzer (AATI) and NanoDrop ND-1000 (Wilmington), respectively. The mRNA was isolated from 2 ug of total RNA using the NEBNext Poly (A) mRNA Magnetic Isolation Module. Subsequently, isolated mRNA was used for RNA library construction using NEBNext ultra RNA library prep kit for Illumina. The generated libraries were pooled and sequenced on Illumina HiSeq 4000 platforms with paired-end 150-bp sequencing.

RNA-seq Data Analysis

Raw reads with low-quality bases (N > 10%) and adaptor contaminants were removed, and the clean reads were mapped to hg19 human reference (UCSC) using TopHat (version 2.0.12) (Trapnell et al., 2009; Trapnell et al., 2012). According to SAM files and GTF files, gene count expression level was analyzed by htseq-count developed with HTSeq (version 0.6.0) (Anders et al., 2015). The transcripts were assembled and normalized using Cufflinks (version 2.2.1) with default parameters (Trapnell et al., 2010; Trapnell et al., 2012). Next, differentially expressed transcripts and genes were analyzed by using the DESeq2 package as previously described (Cole et al., 2012). Genes with significant q-values < 0.05 and fold change > 1.5 or < 1.5^{-1} were selected as differentially expressed genes. Volcano plots were generated using R package ggplot2. Heatmaps were plotted using the pheatmap package in R. Gene Ontology for enrichment analysis was carried out by Gene Ontology Consortium (http://www.geneontology.org/). Polygon Frequency Graph was shown based on $\log_2$ mRNA expression fold changes between *FOXO3*$^{2SA/2SA}$ and *FOXO3*$^{+/+}$ hVECs, hVSMCs and hMSCs (P3) (class interval = 0.1). Briefly, we filtered these genes whose q-values and $\log_2$ fold change were set to NA (not available), and divided the remaining differentially expressed genes between *FOXO3*$^{2SA/2SA}$ and *FOXO3*$^{+/+}$ hMSCs (P3) into 'FOXO3 targets' and 'Non FOXO3 Targets' based on the target genes of *FOXO3* transcription factor ("FOXO3 targets" in Figure 4J) from the CHEA Transcription Factor Targets dataset through low- or high-throughput transcription factor functional studies (http://amp.pharm.mssm.edu/Harmonizome/gene_set/FOXO3/CHEA+Transcription+Factor+Targets).

PPI Network Analysis and Pathway Enrichment Analysis

560 upregulated genes (*FOXO3*$^{2SA/2SA}$ versus *FOXO3*$^{+/+}$ hMSCs, Fold change > 1.5, q < 0.05) and gene *FOXO3* were combined to perform PPI network analysis and pathway enrichment analysis. PPI network analysis was performed with Integrated interactions database (IID) with only "exp- Evidence.Type" PPI used (http://ophid.utoronto.ca/iid) (Kotlyar et al., 2016). Pathway enrichment analysis was performed using pathDIP (version 3.0) (http://ophid.utoronto.ca/pathDIP/) (Rahmati et al., 2017). Both results were visualized using NAViGaTOR (version 3.0) (Brown et al., 2009).

Identification of Tumor Suppressor Genes

All the tumor suppressor genes (TSGs) mentioned in this study were obtained from TSGene 2.0 (https://bioinfo.uth.edu/TSGene/index.html), a comprehensive resource for pan-cancer analysis of human tumor suppressor genes (TSGs) (Zhao et al., 2013).

DNA Library Construction and Sequencing

Genomic DNA extraction was performed according to the DNeasy Blood & Tissue Kit protocol and quantified with the Qubit dsDNA HS Assay Kit. 500 ng of DNA was sheared into approximately 300-bp fragments by Covaris S2. The DNA library was constructed using a NEBNext ultra DNA library prep kit for illumina. The libraries were pooled and subjected to 150-bp paired-end sequencing on Illumina HiSeq 4000 sequencers.

Copy Number Variation (CNV) Analysis

Paired end reads generated from whole-genome DNA sequencing were aligned to hg19 human reference genome by bowtie2 (version 2.2.3). The wild-type samples without CNVs were selected as standard controls. The CNVs were calculated with HMMcopy (version 1.21.0) by estimating the copy number in each 1Mb window (Ha et al., 2012). The CNV plots were generated with package circlize in R.

PBAT Library Construction and Sequencing

Samples of 50 ng of genomic DNA were used to construct the PBAT library as previously described with some modifications (Clark et al., 2017; Smallwood et al., 2014). Briefly, together with 1% unmethylated lambda DNA, genomic DNA was bisulfite converted and purified with EZ-96 DNA Methylation-DirectMagPrep according to the manufacturer's instructions. The bisulfite-converted DNA was subjected to four rounds of random priming and extension with biotinylated random primers containing a truncated Illumina P5 adaptor and supplemented with klenow (3′ → 5′ exo-) polymerase. The excess primers were digested by exonuclease I. After purification of DNA with 0.8 × Ampure XP beads, the newly synthesized DNA strands were bound to the Dynabeads M280 Streptavidin and the bisulfite-converted DNA templates were removed with two rounds of 0.1 N NaOH washes. The second strands were then synthesized with random primers containing a truncated P7 Illumina adaptor. The M280 beads were washed again and the library was amplified with KAPA HiFi ReadyMix (Kapa biosysems) for 6-8 cycles. The generated libraries were purified twice with 0.8 × Ampure XP beads and sequenced on Illumina HiSeq 4000 sequencers to generate 150-bp paired-end reads.

PBAT Data Quality Control and Alignment

Raw reads were first trimmed of 9 bases of random primers and contaminated adaptors, and reads with low-quality bases were discarded using trim_galore (version 0.3.3). Next, the clean reads were aligned to the hg19 human reference genome by bismark (version 0.7.6) (Krueger and Andrews, 2011) using our analysis pipline (Zhu et al., 2018). After alignment, PCR duplificates were removed using SAMtools (Li et al., 2009). Samples with bisulfite conversion rate of lambda DNA greater than 99% were used for subsequent DNA methylation analysis.

DNA Methylation Level Estimation

After read alignments to the genome, the methylated and unmethylated reads were calculated based on the covered cytosine (reported as C) sites and thymine (reported as T) sites in the same reference position, respectively. The DNA methylation levels were estimated by the ratios of the methylated reads to the total reads. Unless noted otherwise, all the descriptions of the DNA methylation levels of any given sample were referred to as the DNA methylation levels on CpG sites of this sample.

QUANTIFICATION AND STATISTICAL ANALYSIS

The statistical analysis was performed and analyzed by Student's t test or one-way ANOVA in Graphpad Prism 6.0 software. Data are presented as mean ± SEM or mean ± SD. p value < 0.05, p value < 0.01 and p value < 0.001 were considered statistically significant (*, **, ***).

DATA AND SOFTWARE AVAILABILITY

The sequencing data have been deposited in the NCBI Gene Expression Omnibus (GEO) under the accession number GEO: GSE116277. All data supporting the findings are available from the Lead Contact upon reasonable request.